universe

MDPI

Article

A Study on the Evolution of Emission Altitude with Frequency Among 104 Normal Pulsars

Chaoxin Luo [1,2], Xin Xu [1,2,3], Changrong Du [1,2] and Qijun Zhi [1,2,*]

[1] School of Physics and Electronic Science, Guizhou Normal University, Guiyang 550025, China; luocx@gznu.edu.cn (C.L.); xinxu@gznu.edu.cn (X.X.); duchangrong24@mails.ucas.ac.cn (C.D.)
[2] Guizhou Provincial Key Laboratory of Radio Astronomy and Data Processing, Guizhou Normal University, Guiyang 550025, China
[3] School of Mathematical Science, Guizhou Normal University, Guiyang 550025, China
* Correspondence: qjzhi@gznu.edu.cn

Abstract: Utilizing the databases from the European Pulsar Network (EPN), the Australia Telescope National Facility (ATNF), and published literature data, a geometric method was used to investigate the multifrequency emission altitude of 104 pulsars. We found that the evolution of emission altitudes with frequency for the majority of pulsars can be fitted using a power-law function with a normalization constant. In this work, it is found that the frequency evolution of pulsar emission altitude can be divided into three groups according to their different frequency dependencies of emission altitude (emission altitude decreases with frequency (Group A, $\eta \leq -0.1$), keeps relatively constant with frequency (Group B, $-0.1 < \eta \leq 0.1$), and increases with frequency (Group C, $\eta \geq 0.1$)), where η is the emission altitude variation rate. We also computed the emission altitudes across multiple frequency bands for these pulsars, thereby estimating the approximate range of the pulsar emission regions. We found that most pulsar emissions occur at altitudes of tens to hundreds of kilometers above the polar cap, with differences in emission altitude between the three groups becoming more clear at lower frequencies.

Keywords: methods; statistical pulsars; pulsars; general pulsars

Academic Editors: Kinwah Wu and Ellis R. Owen

Received: 29 November 2024
Revised: 7 January 2025
Accepted: 10 January 2025
Published: 12 January 2025

Citation: Luo, C.; Xu, X.; Du, C.; Zhi, Q. A Study on the Evolution of Emission Altitude with Frequency Among 104 Normal Pulsars. *Universe* **2025**, *11*, 17. https://doi.org/10.3390/universe11010017

1. Introduction

Since the discovery of the first pulsar [1], about 3700 pulsars have been discovered. (according to version 2.5.1 of the ATNF Catalog [2], available here: www.atnf.csiro.au/people/pulsar/psrcat/, accessed on 1 November 2024) Various models have been put forward to interpret the different observational phenomenology and physical mechanisms of pulsars [3–6]. Goldreich and Julian [7] were the first to propose that a charge-separated magnetosphere surrounds a neutron star. Ruderman and Sutherland ([4], hereafter referred to as the RS model) proposed the existence of an acceleration region above the pulsar's polar cap (an area enclosed by critical magnetic field lines), where high-energy particles are accelerated and then flow outward along the magnetic field lines, producing observable radio emissions through the process of curvature emissions. In the curvature emission (CR) model, the emission beam is generally considered to be a single conical component. Therefore, the pulse profile should consist of either a single peak or a double peak [4,8]. In some studies, core emissions in the CR model have also been discussed [9,10]. This can explain the pulse profiles of some pulsars, but the RS model also has limitations in interpreting multi-component pulse profiles. To comprehend the diversity of pulse profiles, previous research has proposed several geometric models, such as the "core–cone" beam, the "core–double

cone" beam, the fan beam, and the microbeam [4,6,11–13]. The Inverse Compton Scattering (ICS) model possesses unique advantages in explaining multi-component profiles. In the ICS model, the radio emission from pulsars results from the scattering of secondary particles from "low-frequency" waves. The emission beam comprises a core and two conical components; thus, the number of pulse peaks can range from 1 to 5 [5,14]. These models have their own advantages in explaining some observed characteristics. However, a complete consensus on the emissions mechanism of pulsars has not yet been reached.

Multi-band observations are very important for understanding the physical properties of pulsars. Radio emissions at different frequencies are believed to originate from varying emission altitudes [15], and the study of multi-band data can reveal the range of variations in the pulsar's emission regions [16], which aids in constraining the geometry of the emission beam. To pinpoint the location of pulsar radio emission sources within the magnetosphere, previous studies have proposed various methods for estimating the altitude of radio emissions [17–22]. Currently, there are three main methods used for calculating emission altitude: (1) a relativistic rotating vector model ([22], BLW); (2) the relativistic phase shift method ([18,23], GRT); (3) the geometric method ([20,24], KG). The first method takes into account aberration and retardation (A/R) effects. The relativistic motion of the emission region relative to the observer as the region co-rotates with the pulsar causes aberration and retardation [25]. This effect causes a delay in the pulse phase of the inflection point of the PA curve predicted by RVM relative to the location of the fiducial plane inferred from the intensity profile. This means we need to make polarization observations. The second method also considers the influence of the A/R effect, assuming that if the core originates from a lower height than the cone and the cone is axially symmetric around the core in a reference frame co-rotating with the star, then the core component will experience a phase lag at the midpoint between the maximum cone components. The third method assumes that the emission originates from the outermost open field line and involves comparing the measured pulse width with the geometric predictions derived from a dipole model.

Each of these three methods has its own advantages and disadvantages. The first method requires fewer assumptions and involves simpler calculations. The second method allows for the separate calculation of the emission altitude of the core and cone components. Both methods necessitate high-quality polarization data. However, it has been established that depolarization emitted by pulsars occurs at high frequencies [26]. The low signal-to-noise ratios imposed by this depolarization at high frequencies leads to a broad scatter in the values of the polarization position angle curve, thus making the fitting procedure difficult. Furthermore, the second method relies on clear identification of the core-cone structure, with the average profile necessitating a certain degree of asymmetry. For such analyses, a three-component or double-cone profile is most ideal. Therefore, if there is no clear core-cone structure present, the method cannot be applied. The advantage of the third method lies in its capability of calculating the emission altitude at corresponding frequencies using pulse widths of different wavebands, after determining the geometric parameters (such as inclination angle α and impact angle β.) of the pulsar. Therefore, it is often used in studies of pulsar emission–frequency relationships [16,24]. However, it is noteworthy that the actual emission might not come from the final open field line. Therefore, assigning the edge of the intensity contour to the final open magnetic field line could lead to misinterpretation, causing the calculated emission height to be lower than the actual one. Additionally, since α and β are unobservable quantities and contain errors in the calculation process, using the KG method does not give us the absolute emission height; it only represents the lower limit of the emission height for that frequency band.

Previous studies have attributed the decreasing trend of emission altitude with frequency to the scenario of narrowband emissions, specifically through radius-to-frequency mapping ([15], RFM) based on the RS model. This power-law dependence typically assumes that high-frequency radio emissions originate from regions closer to the surface of the neutron star, whereas the opposite is true for lower frequencies. Kijak and Gil ([16], KG98) use a geometric method to calculate the emission altitude across multiple wavebands for multiple pulsars. They believe that the emission frequency follows an RFM relationship, which can be expressed as a power-law function in the form of $r_6 = A\nu^{\alpha}$. The calculation using the geometric method is conducted by assuming that the edges of the average profile originate from the last open field line. The frequency dependence is highly correlated with the frequency dependence of pulse width. Current research suggests that the evolutionary relationship between pulse width and frequency cannot be fully described by a single power-law function alone. Rather, it should be characterized by multiple power-law functions [27] or by the relationship $\triangle\theta = A\nu^{-\alpha} + \triangle\theta_{min}$ [28,29]. Furthermore, in addition to conforming to the RFM model, the evolution of emission altitude with frequency also exhibits a pattern where the emission altitude increases as the frequency rises [30]. Therefore, there is a necessity for new research into the frequency-altitude relationship in pulsar emissions.

In recent years, several studies have presented the observational results of pulsar emissions at lower and higher frequencies [31–33], and geometric parameters of the beams emitted by pulsars [34,35]. This makes it possible to study the multi-band evolution of the emission altitude of pulsars using geometric methods. In this work, utilizing datasets from the European Pulsar Network (EPN) and the Australian Telescope National Facility (ATNF), supplemented by data from the published literature, a comprehensive survey was conducted on the emission altitudes of 104 normal pulsars with multifrequency (40 MHz–10.55 GHz) observational data. We attempted to uncover the frequency evolution behavior of the emission altitude of these pulsars. The structure of this paper is as follows: In Section 2, we present information on the data used in this paper. In Section 3, the methodology used for calculating the emission altitude and pulse width is elaborated upon in detail. In Section 4, the research results are presented. Finally, a discussion and our conclusions are presented in Section 5.

2. Information on the Data

From the EPN and ATNF databases, as well as some recently published datasets, we obtained high signal-to-noise ratio multifrequency observational data for 104 pulsars. The data sources for all pulsars are listed in Table 1. To select the required multifrequency observational data, we followed these steps:

(1) Firstly, pulsar data with multifrequency observations and an observation frequency range greater than 1 GHz were selected from the EPN and ATNF databases to form the initial sample. The pulsar periods (P) from the initial sample were obtained from the ATNF database, and the geometric parameters (such as α and β) for the pulsars in the initial sample were collected by searching the published literature. Pulsars without relevant parameters were discarded.

(2) Subsequently, multifrequency average profiles were plotted for the data selected from EPN and ATNF. Gaussian fitting was applied to these average profiles to calculate the W_{10} values for each frequency band. Data from frequency bands with excessively low signal-to-noise ratios ($S/N \leq 15$) that made W_{10} determination difficult were discarded, as were data showing significant scattering phenomena [36].

(3) In addition to this, we collected information on the pulse widths of these pulsars from the reference dataset, which was used to extend the frequency range to make

the results more accurate. It is worth noting that in many cases, there are different observations at the same frequency. For this, we chose the one with the better signal-to-noise ratio as well as the one with the closer observation time. In the case of the results in Refs. The errors come from the corresponding reported articles.

(4) Pulsars with more than four multifrequency data points and observation frequencies spanning 1 GHz were retained after the above screening steps. And the maximum observation frequency was as many times larger than the minimum observation frequency as possible.

Based on the selection criteria outlined above, we screened a total of 104 pulsars. We applied the least-squares fitting method to the radiation–frequency relationship of these sample pulsars using Equation (4) (detailed calculations are provided in Section 3). It is noteworthy that between different modes, variations in the average profile shapes can lead to changes in the emission altitude calculated using KG. This paper only considers the average profiles in the normal mode as the baseline for calculating the emission altitude.

Table 1. References for the pulse width data used in this paper. The first column gives the names of the pulsars, and the numbers in the second column represent their observation frequency. The superscript indicates the origin of the data, where "^{e}" represents the data is from EPN and "^{a}" represents the data is from ATNF.

PSR B	Frequency (MHz)
B0031−07	38 [34] 60 [12] 64.5 [33] 79.2 [33] 102.5 [11] 150 [26] 185 [14] 230 [7] 333 [22] 350 [26] 400 [7] 607 [14] 800 [16] 950 [35] 1284 [32] 1412 [12] 1500 [26] 3094 [a] 4850 [e]
B0052+51	129 [e] 168 [e] 400 [7] 600 [7] 1408 [e] 1642 [e] 4850 [e]
B0105+65	129 [e] 168 [e] 408 [e] 610 [e] 1400 [13] 1642 [e]
B0136+57	230 [7] 400 [7] 610 [e] 920 [7] 1250 [18] 1400 [7] 1600 [7] 4750 [e]
B0138+59	40 [26] 103 [e] 150 [26] 350 [26] 600 [7] 925 [e] 1400 [7] 1500 [26] 1642 [e] 4850 [28]
B0149−16	35.1 [33] 49.8 [33] 64.5 [33] 230 [7] 333 [22] 400 [7] 618 [22] 720 [a] 950 [35] 1284 [32] 1400 [7] 2368 [a] 3100 [a]
B0254−53	434 [e] 636 [21] 950 [35] 1284 [32] 1560 [e]
B0301+19	129 [e] 150 [26] 327 [24] 400 [7] 618 [22] 920 [7] 1284 [32] 1500 [26] 4600 [24]
B0331+45	150 [26] 350 [26] 408 [e] 600 [7] 1250 [18] 1400 [7] 1500 [26]
B0402+61	150 [26] 230 [7] 350 [26] 400 [7] 600 [7] 1400 [7] 1500 [26] 1600 [7] 4850 [28]
B0410+69	150 [26] 350 [26] 400 [7] 600 [7] 925 [e] 1400 [7] 1500 [26]
B0450+55	40 [26] 65 [e] 129 [e] 400 [7] 920 [7] 1250 [18] 4820 [39]
B0450−18	408 [e] 600 [7] 920 [7] 1250 [18] 1400 [7] 1600 [7] 4850 [e]
B0458+46	333 [22] 408 [e] 631 [21] 950 [35] 1284 [32] 1642 [e] 4850 [28]
B0523+11	327 [24] 350 [26] 400 [7] 600 [7] 800 [e] 920 [7] 1400 [24] 1500 [26] 1600 [7] 4600 [24]
B0525+21	40 [26] 150 [26] 230 [7] 327 [24] 333 [22] 350 [26] 400 [7] 600 [7] 920 [7] 1400 [24] 1500 [26] 1600 [7] 1710 [e] 3100 [a] 4600 [24] 4820 [39]
B0540+23	230 [7] 327 [24] 400 [7] 618 [22] 732 [a] 900 [7] 1250 [18]3094 [a] 4820 [39] 8500 [e] 10550 [16]
B0559−05	400 [7] 600 [7] 732 [a] 800 [e] 920 [7] 1284 [32] 1400 [7] 1600 [7] 3094 [a] 4850 [28]
B0609+37	150 [26] 350 [26] 400 [7] 600 [7] 920 [7] 1400 [7] 1500 [26] 1600 [7] 4600 [24] 4850 [28]
B0611+22	333 [22] 400 [7] 610 [e] 900 [7] 1250 [2] 1600 [7] 4850 [e]
B0626+24	129 [e] 230 [7] 327 [24] 400 [7] 618 [22] 925 [e] 1284 [32] 1400 [7] 1600 [7] 4600 [24] 4850 [28]
B0628−28	35.1 [33] 49.8 [33] 64.5 [33] 79.2 [33] 102.5 [11] 230 [7] 400 [7] 649 [21] 719 [a] 800 [35] 950 [35] 1284 [32] 1400 [7] 1600 [7] 3094 [a] 4850 [28] 10550 [e]
B0656+14	149 [e] 327 [24] 400 [7] 600 [7] 610 [e] 732 [a] 1250 [18] 1284 [32] 1400 [24] 1600 [7] 3094 [a] 4600 [24] 4850 [e] 6200 [a]
B0727−18	333 [22] 400 [7] 618 [22] 900 [7] 1284 [32] 1400 [7] 1600 [7]
B0736−40	631 [21] 674 [e] 728 [a] 950 [35] 1284 [32] 1465 [a] 3100 [e] 4543 [e] 4820 [39] 8600 [38]
B0740−28	333 [22] 400 [7] 631 [21] 732 [a] 950 [35] 1284 [32] 1400 [7] 1526 [a] 1600 [7] 3100 [e] 4820 [39] 6200 [a] 10550 [e]
B0751+32	102.5 [11] 149 [e] 327 [24] 400 [7] 600 [7] 910 [e] 1400 [24] 4600 [24] 4850 [28]
B0809+74	64 [e] 102 [4] 110 [36] 150 [17] 230 [7] 350 [26] 606 [e] 920 [7] 1330 [16] 1400 [7] 1500 [26] 1600 [7] 4850 [28] 10550 [28]
B0818−13	58.6 [33] 149 [e] 150 [26] 333 [22] 618 [22] 950 [35] 1600 [7] 3094 [a] 4820 [39]
B0820+02	135 [e] 230 [7] 350 [26] 400 [7] 600 [7] 920 [7] 1284 [32] 1382 [a] 1500 [26] 1600 [7]
B0823+26	38 [e] 40 [26] 64.5 [33] 79.2 [33] 102 [e] 150 [26] 327 [24] 408 [e] 610 [e] 925 [e] 1420 [16] 1500 [26] 4600 [24] 4820 [39] 10550 [16]
B0834+06	35.1 [33] 40 [26] 49.8 [33] 64.5 [33] 79.2 [33] 102.5 [11] 327 [24] 400 [7] 618 [22] 728 [a] 950 [35] 1284 [32] 1400 [24] 1500 [26] 4600 [24]
B0844−35	315 [30] 333 [22] 433 [30] 600 [7] 950 [35] 1284 [32] 1440 [e]
B0906−17	78.2 [33] 150 [26] 230 [7] 400 [7] 600 [7] 1400 [7] 1500 [26] 1600 [7] 4850 [28]
B0917+63	40 [26] 150 [26] 230 [7] 350 [26] 400 [7] 600 [7] 1400 [7] 1500 [26]
B0919+06	103 [e] 150 [26] 350 [26] 600 [7] 950 [35] 1284 [32] 1400 [24] 1500 [26] 1600 [7] 1710 [e] 3100 [a] 4600 [24] 4750 [16] 6200 [a] 8356 [e] 10550 [16]
B0940−55	631 [21] 1284 [32] 1383 [e] 3100 [a]
B0942−13	230 [7] 900 [7] 1560 [e] 4850 [28]
B0943+10	40 [26] 65 [e] 150 [26] 350 [26] 400 [20] 728 [a] 1500 [26]
B0950+08	38 [e] 151 [e] 327 [24] 618 [22] 950 [35] 1284 [32] 1400 [24] 1500 [26] 3100 [a] 4600 [24] 4750 [16] 4820 [39] 6200 [a] 8600 [38] 10550 [16]
B1039−19	400 [7] 600 [7] 800 [e] 920 [7] 1284 [32] 1600 [7] 4850 [28]
B1112+50	40 [26] 150 [26] 350 [26] 600 [7] 920 [7] 1500 [26] 1642 [e]
B1133+16	35.1 [33] 49.8 [33] 64.5 [33] 79.2 [33] 150 [26] 327 [24] 600 [7] 950 [35] 1284 [32] 1710 [e] 2250 [e] 3100 [a] 4750 [16] 8600 [38] 10550 [16]
B1237+25	40 [26] 103 [e] 150 [26] 333 [22] 638 [21] 920 [7] 1284 [32] 1500 [26] 3100 [a] 4600 [24] 4820 [39]
B1325−43	435 [e] 618 [22] 1284 [32] 1369 [e] 1560 [e]
B1451−68	450 [e] 649 [21] 950 [35] 1284 [32] 1369 [e] 1520 [e] 8356 [e]
B1508+55	58.6 [33] 78.2 [33] 102.5 [11] 159 [e] 350 [26] 600 [7] 920 [7] 1500 [26] 1642 [e] 4820 [39]
B1530+27	103 [e] 150 [26] 230 [7] 327 [24] 400 [7] 600 [7] 920 [7] 1400 [24] 1500 [26] 1642 [e] 4600 [24]
B1540−06	40 [26] 64.5 [33] 150 [26] 350 [26] 732 [a] 920 [7] 1284 [32] 1500 [26] 4750 [e]

Table 1. *Cont.*

PSR B	Frequency (MHz)
B1556−44	333 [22] 631 [21] 950 [35] 1284 [32] 1560 [e] 3200 [a] 4820 [39]
B1604−00	35.1 [33] 49.8 [33] 64.5 [33] 79.2 [33] 103 [e] 230 [7] 350 [26] 631 [21] 950 [35] 1284 [32] 1600 [7] 4850 [28]
B1612+07	35.1 [33] 64.5 [33] 102.5 [11] 150 [15] 327 [24] 600 [7] 1284 [32] 1500 [26] 4600 [24]
B1633+24	40 [26] 168 [e] 327 [24] 600 [7] 1400 [24]
B1642−03	49.8 [33] 64.5 [33] 79.2 [33] 103 [e] 324 [23] 631 [21] 920 [7] 1420 [16] 3094 [a] 4820 [39] 8600 [38] 10550 [16]
B1649−23	400 [7] 600 [7] 920 [7] 1400 [7] 1640 [7] 4850 [e]
B1700−32	49.8 [33] 64.5 [33] 79.2 [33] 333 [22] 618 [22] 950 [35] 1284 [32] 1369 [e]
B1706−16	49.8 [33] 64.5 [33] 79.2 [33] 102.5 [11] 270 [21] 400 [7] 618 [22] 920 [7] 1284 [32] 1420 [16] 1600 [7] 2650 [22] 3094 [a] 4750 [16] 8600 [38] 10550 [16]
B1706−44	450 [e] 1280 [32] 1440 [e] 5124 [39] 8600 [38]
B1717−29	333 [22] 400 [7] 600 [7] 618 [22] 1284 [32] 1600 [7] 4850 [28]
B1718−32	400 [7] 638 [21] 950 [35] 1284 [32] 1369 [29] 1642 [e]
B1737−30	920 [7] 1400 [7] 1600 [7] 4850 [e] 5124 [39] 8356 [e]
B1738−08	400 [7] 600 [7] 920 [7] 1284 [32] 1600 [7] 4850 [e]
B1749−28	149 [e] 350 [26] 618 [22] 925 [e] 1284 [32] 1600 [7] 2878 [a] 4820 [39] 8600 [38]
B1804−08	400 [7] 618 [22] 950 [35] 1284 [32] 1500 [26] 3100 [e] 4820 [39] 8600 [38]
B1819−22	333 [22] 600 [7] 920 [7] 1400 [7] 1600 [7] 4850 [28]
B1826−17	660 [e] 950 [35] 1284 [32] 1400 [7] 5124 [39] 8600 [38]
B1831−04	103 [e] 333 [22] 400 [7] 618 [22] 920 [7] 1284 [32] 1500 [26] 1600 [7] 4850 [28]
B1839+09	129 [e] 327 [24] 618 [22] 920 [7] 1250 [18] 1284 [32] 1400 [24] 1500 [26] 1642 [e] 4600 [24] 4850 [28]
B1839+56	65 [e] 103 [e] 408 [e] 600 [7] 920 [7] 1400 [7] 1600 [7] 4850 [e]
B1845−01	618 [22] 950 [35] 1250 [18] 1400 [7] 1642 [e] 3100 [a] 4750 [16] 5124 [39] 8600 [38] 10550 [16]
B1848+12	129 [e] 327 [24] 600 [7] 1250 [18] 1418 [e] 4600 [24]
B1905+39	102.5 [11] 150 [26] 350 [26] 600 [7] 920 [7] 1410 [e] 1500 [26] 4850 [28]
B1911−04	333 [22] 618 [22] 950 [35] 1600 [7] 3100 [a] 4850 [e]
B1913+167	400 [7] 600 [7] 1284 [32] 1400 [7]
B1914+09	143 [e] 400 [e] 653 [a] 925 [e] 1250 [18] 1500 [26] 1642 [e] 4850 [28]
B1916+14	327 [24] 600 [7] 1250 [18] 1400 [24] 1600 [7] 4600 [24]
B1918+19	400 [e] 610 [e] 920 [7] 1400 [7] 1642 [e]
B1919+21	38 [e] 49.8 [33] 64.5 [33] 79.2 [33] 150 [26] 327 [24] 618 [22] 920 [7] 1250 [18] 1600 [7] 4600 [24]
B1920+21	350 [26] 400 [7] 600 [7] 1250 [18] 1642 [e]
B1923+04	135 [e] 350 [26] 600 [7] 920 [7] 1250 [18] 1500 [26] 1600 [7] 4850 [28]
B1924+16	327 [24] 610 [e] 925 [e] 1250 [18] 1400 [24] 1642 [e] 4600 [24]
B1929+10	150 [26] 333 [22] 400 [7] 618 [22] 950 [35] 1250 [18] 1450 [16] 1600 [7] 2955 [a] 3094 [a] 4600 [24] 4820 [39] 6000 [27] 8600 [38] 10550 [16]
B1935+25	327 [24] 600 [7] 920 [7] 1250 [18] 1400 [24] 1600 [7] 4600 [24] 4920 [39]
B1952+29	102.5 [11] 400 [7] 920 [7] 1400 [24] 1600 [7] 4600 [24] 4920 [39]
B1953+50	40 [26] 150 [26] 400 [7] 600 [7] 920 [7] 1400 [7] 1600 [7] 4920 [39]
B2003−08	400 [7] 600 [7] 920 [7] 1400 [7]
B2016+28	64.5 [33] 102 [12] 230 [7] 327 [24] 400 [7] 610 [12] 920 [7] 1250 [18] 1412 [12] 1600 [7] 4600 [24] 4820 [39] 10550 [e]
B2020+28	58.6 [33] 120 [e] 230 [7] 327 [24] 600 [7] 920 [7] 1250 [18] 1400 [24] 1600 [7] 4600 [24] 4850 [e] 10450 [e]
B2021+51	120 [e] 230 [7] 400 [7] 600 [7] 925 [e] 1250 [18] 1400 [24] 1500 [26] 1710 [e] 4820 [39] 8500 [e] 8600 [38] 10550 [16]
B2044+15	129 [e] 230 [7] 350 [26] 610 [e] 925 [e] 1284 [32] 1500 [26]
B2045−16	102.5 [11] 333 [22] 618 [22] 920 [7] 1284 [32] 1420 [16] 1600 [7] 2955 [a] 4750 [16] 4850 [28] 6200 [a] 8600 [38] 10550 [16]
B2106+44	350 [26] 600 [7] 920 [7] 1400 [7] 1600 [7] 4750 [e]
B2110+27	35.1 [33] 49.8 [33] 64.5 [33] 102.5 [11] 150 [26] 230 [7] 400 [7] 600 [7] 920 [7] 1400 [7] 1500 [26] 1600 [7] 4850 [28]
B2111+46	151 [e] 400 [7] 600 [7] 920 [7] 1225 [9] 1642 [e] 4850 [28]
B2148+63	350 [26] 600 [7] 920 [7] 1400 [7] 1600 [7] 4850 [28]
B2152−31	230 [7] 600 [7] 920 [7] 1284 [32] 1560 [e]
B2154+40	102.5 [11] 150 [26] 230 [7] 350 [26] 600 [7] 925 [e] 1400 [7] 1500 [26] 4850 [28]
B2306+55	129 [e] 230 [7] 400 [7] 600 [7] 920 [7] 1400 [7] 1500 [26] 4850 [e]
B2310+42	102.5 [11] 230 [7] 333 [22] 600 [7] 920 [7] 1400 [7] 1510 [16] 4750 [16] 4850 [28] 10550 [16]
B2315+21	129 [e] 230 [7] 333 [22] 600 [7] 920 [7] 1250 [32] 1400 [7] 4850 [28]
B2319+60	230 [7] 400 [7] 600 [7] 800 [e] 920 [7] 1460 [16] 4750 [16] 4820 [39] 10550 [16]
B2323+63	400 [7] 600 [7] 920 [7] 1408 [e] 1600 [7]
B2324+60	408 [e] 600 [7] 920 [7] 1400 [7] 1600 [7]
B2327−20	64.5 [33] 79.2 [33] 230 [7] 333 [22] 648 [21] 920 [7] 1284 [32] 3094 [a] 4920 [39]
B2351+61	230 [7] 400 [7] 600 [7] 920 [7] 1400 [7] 1600 [7] 4750 [16] 10550 [16]

Notes: ([1]) Arzoumanian, Z [37]; ([2]) Sun, S.N [38]; ([3]) Cañellas, A [39]; ([4]) Davies, J.G [40]; ([5]) Dike, V [41]; ([6]) Gancio, G [42]; ([7]) Gould, D.M [43]; ([8]) Hamilton, P.A [44]; ([9]) Zhi, Q.J [45]; ([10]) Izvekova, V.A [46]; ([11]) Izvekova, V.A [47]; ([12]) Izvekova, V.A [48]; ([13]) Johnston, Simon [49]; ([14]) McSweeney, S.J [50]; ([15]) Keith, M.J [51]; ([16]) Kramer, M [52]; ([17]) Basu, Rahul [53]; ([18]) Wang, P.F [54]; ([19]) Cai, Yanqing [55]; ([20]) Manchester, R.N [56]; ([21]) McCulloch, P.M [57]; ([22]) Mitra, Dipanjan [58]; ([23]) Singh, Shubham [59]; ([24]) Olszanski, Timothy E.E [60]; ([25]) Page, Clive G [61]; ([26]) Pilia, M [31]; ([27]) Chen, J.L [62]; ([28]) Kijak, J [63]; ([29]) Zhao, D [64]; ([30]) Basu, Rahul [65]; ([31]) Kijak, Jaroslaw [16]; ([32]) Posselt, B [66]; ([33]) Stovall, K [32]; ([34]) Tsai, Jr-Wei [67]; ([35]) van Ommen, T.D [68]; ([36]) Vitkevich, V.V [69]; ([37]) Zhou, Zu-Rong [70]; ([38]) Zhao, Ru-Shuang [71]; ([39]) Zhao, Ru-Shuang [33].

3. Methods for Determination of Emission Altitude

The geometric method involves comparing the measured pulse width with the geometric predictions derived from a dipole model [20]. In the polar cap geometric model of pulsars, the emission altitude r_6 can be simply expressed as

$$r_6 = (\rho/1.24^\circ s P^{-0.5})^2, \quad (1)$$

where P is the pulsar's spin period, and $r_6 = r/10^6$ cm is the emission altitude. The parameter s lying in the range of $0 \leq s \leq 1$ describes the locus of the field line at the polar

cap, where $s = 0$ at the magnetic pole and $s = 1$ at the edge of the Goldreich-Julian [7] circular polar cap and the radius of the pulsar. In our work, we assume $s = 1$. ρ is the opening angle of the emission beam, which can be expressed as

$$\rho = 2 \arcsin\left\{ \sqrt{\sin^2 \frac{W}{4} \sin\alpha \sin(\alpha + \beta) + \sin^2 \frac{\beta}{2}} \right\}, \quad (2)$$

where α is the magnetic inclination angle and β is the impact angle of the line of sight, which can be obtained from some published literature [6,12,34,35,72,73]. W is the width of the pulse profile, usually denoted by W_{50} or W_{10}. Due to the presence of multiple components in the average profiles of many pulsars, at certain frequencies, the amplitude of a particular emission component may drop below half of the maximum peak height, leading to a discontinuity in W_{50} [74,75]. To mitigate this effect, we use W_{10} to represent the pulse width of the average pulse profile, which is measured at the 10% level of the maximum peak height in the pulse profile. If the utilization of W_{10} remains unable to mitigate the impact of absorption phenomena, we will refrain from utilizing the data from that pulsar.

For the data from EPN and ATNF, W_{10} is determined by using multiple Gaussian functions to fit the profile [75–77]. The multiple Gaussian functions are defined by the equation

$$y = \sum_{i=1}^{n} A_i \exp\left[-4 \ln 2 \left(\frac{(x - p_i)^2}{w_i^2} \right) \right], \quad (3)$$

where A_i, p_i, and w_i are the amplitude, peak position, and FWHM of the i^{th} Gaussian component, respectively. The errors of W_{10} are estimated with the method provided in Ref. [78].

To describe the relationship between emission altitude and frequency, we choose to adopt the form of a power-law function with an added constant, expressed as

$$r_6 = A\nu^n + C, \quad (4)$$

here, r_6 represents the emission altitude, ν denotes the frequency, A and C are constants, and n is the frequency-dependent index for the emission altitude. The weighted Levenberg–Marquardt nonlinear least-squares fitting algorithm is employed to determine the best-fit A, c, and index n. Both A and C are constrained to be non-negative. To estimate the parameter uncertainties at the 95% confidence level, the parameter space that fulfills the condition $\chi^2 \leq \chi^2_{\text{min}} + \Delta\chi^2$ is identified. The exploration of the parameter space is conducted within linearly spaced grids centered around the optimized values of the three parameters. Here, χ^2_{min} denotes the minimized chi-square value, and $\Delta\chi^2$ corresponds to the chi-square increment for the 95% confidence level, given a degree of freedom of $N - 3$, where N is the number of data points for each pulsar and 3 represents the number of free model parameters [79].

4. Results

By using the least-squares method, we obtained the evolution equations for the emission altitudes of 104 pulsars as a function of frequency. The fitting parameters and their 95% confidence intervals are presented in columns 5 to 7 of Table 2. Since no single parameter from A, n, or C is sufficient to determine the evolution of pulsar emission altitude with frequency, we chose to classify the pulsars by calculating the rate of change in emission altitude, denoted as η ($\eta = (r_{4850\,\text{MHz}} - r_{40\,\text{MHz}})/r_{40\,\text{MHz}}$). Here, $r_{40\,\text{MHz}}$ and $r_{4850\,\text{MHz}}$ are the emission altitude calculated at the corresponding frequencies using the optimal parameters from the fitting formula (EP (4)). In the left panel of Figure 1, the distribution of η provides

a clear demonstration of the differences in the frequency evolution of emission altitude among the three pulsar groups. Based on variations in η, we classified pulsars into these three categories: A, B, and C. Pulsars in Group A exhibit negative n-values (Group A, $\eta < -0.1$), with their emission altitude decreasing significantly as frequency increases. This group comprises 88 pulsars, accounting for 85% of the total sample. Pulsars in Group B are more concentrated around 0 (Group B, $-0.1 < \eta < 0.1$), with their emission altitude remaining relatively constant as frequency increases. Pulsars in Group C have positive n-values (Group C, $\eta > 0.1$), and their emission altitude increases with increasing frequency. Each of these two groups contains eight pulsars, representing 7.5% of the total sample. We also plotted a histogram displaying the distribution of the exponent n. In the right panel of Figure 1, the majority of the best-fit n values are continuously distributed and peak near -0.5. The plots illustrating the relationship between emission altitude and frequency for each group are shown in Figures 2–4. Circles represent the results from the published literature, stars denote the results from ATNF, and triangles indicate the results from EPN. The blue solid line represents the weighted fitting curve for the emission altitude. Now, we will proceed to present a detailed discussion of our results.

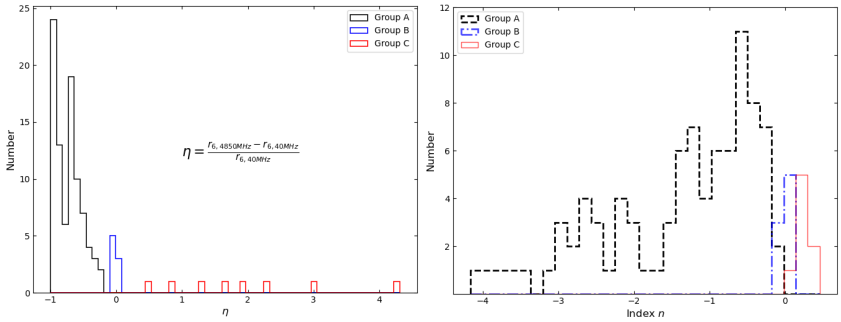

Figure 1. The right panel of the figure shows a histogram of the n-index distribution, while the left panel displays a histogram of the emission altitude change rate (η). The colors indicate group membership: black for Group A, blue for Group B, and red for Group C.

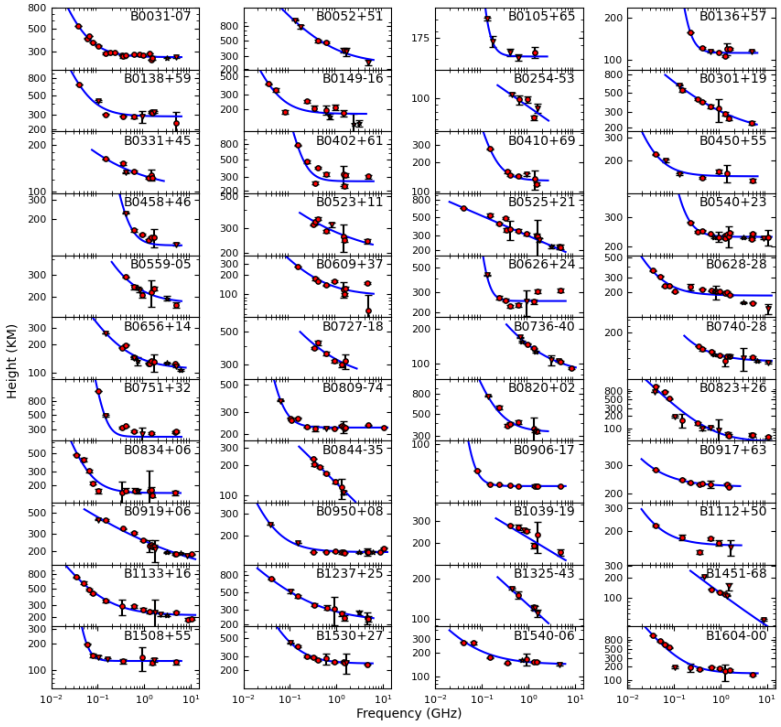

(**a**)

Figure 2. *Cont.*

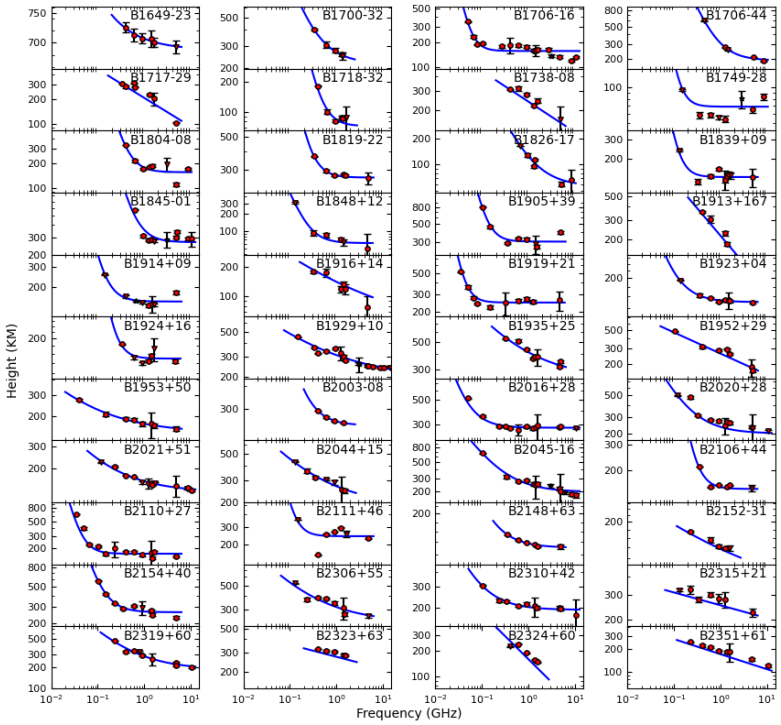

(**b**)

Figure 2. (**a**) The multifrequency research results of the emission altitudes of the first 44 pulsars among the 88 pulsars in Group A. (**b**) The multifrequency research results of the emission altitudes of the last 44 pulsars among the 88 pulsars in Group A. The vertical axis in the figure represents the emission altitude, with the unit being km. Circles represent data from the references, stars represent data from ATNF, and triangles represent data from EPN. The solid black line represents the formal weighted fit to the data points, and the error bars reflect the uncertainty of the emission altitude measurements.

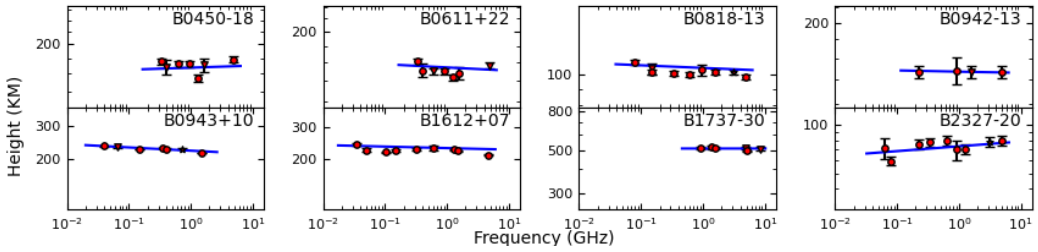

Figure 3. Results of a multiple-frequency study of emission altitudes for Group B in 8 pulsars.

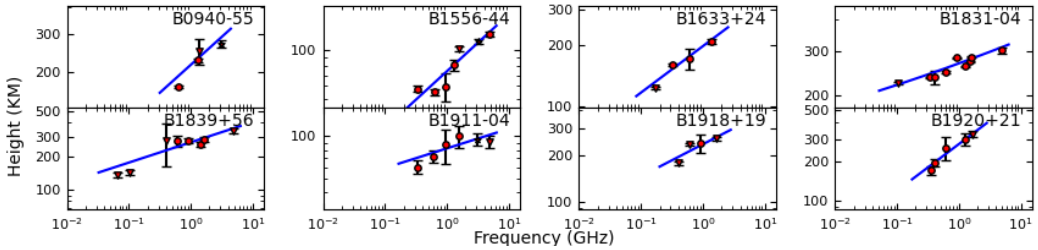

Figure 4. Results of a multiple-frequency study of emission altitudes for Group C in 8 pulsars.

4.1. Group A

In our study, group A pulsars make up the largest proportion, with the fitting results shown in Figure 2. The emission altitude of pulsars in this group decreases significantly with increasing frequency, consistent with the RFM model. Previous studies suggested that the emission height–frequency relationship could be represented by a power-law

function in the form of $r_6 = A\nu^{\alpha}$ [16]. However, in our research, we found that for most pulsars in group A, the emission altitude tends to stabilize at high frequencies, while at low frequencies, the emission altitude exhibits more dramatic variations, especially below 300 MHz. The evolutionary behavior in such cases is difficult to explain using a single power-law function. For this type of pulsar, the emission height–frequency relationship can be better described by a power-law function plus a constant.

There exist some pulsars in Group A within our frequency range that do not demonstrate the characteristic behavior of stabilizing at high frequencies. A prominent distinction among these pulsars is that their fitting parameter C approaches zero. This may be due to the insufficiently broad observational frequency band of these pulsars. For instance, pulsars such as B0254−53, B0736−40, and B0844−35, based on the general trend observed in pulsars with broader frequency bands in Group A, may undergo more rapid changes in their emission intensities at low frequencies. However, this requires further observations to confirm. The statistical results indicate that for pulsar group A, in frequency bands of 300 MHz–10.55 GHz, the variation in the emission altitude does not exceed 500 km, and the variation range of the emission altitude for most pulsars is mainly concentrated within 300 km. We also calculated the average value of pulsar parameter C for those pulsars whose emission altitudes converge at high frequencies, and found that the average asymptotic emission altitude at high frequencies for pulsar group A is approximately 178 km. This indicates that high-frequency emissions (above 4.85 GHz) originate from regions 100–200 km above the neutron star. It is noteworthy that for many pulsars belonging to the A class, regarding the emission altitude calculated using geometric methods at low frequencies (below 300 MHz), the variation range can also be larger than the previously assumed 500 km.

4.2. Group B

In our sample, there are only eight pulsars in group B, and the results are shown in Figure 3. The fitting results show that their index n approaches 0, meaning that the emission altitude remains almost constant over a broad frequency range. The statistical results indicate that the variation range of emissions for the eight pulsars in Group B within the known frequency bands is less than 40 km. This indicates that the emission region is compact, and the radius of the emission beam changes very little or not at all with frequency.

In group B, some pulsars have narrower data frequency ranges, such as B0450−18, B0611+22, B0942−13, and B1737−30. However, for these pulsars, due to the lack of low-frequency observational data, we cannot confirm whether they exhibit similar rapid changes in emission altitude at frequencies below 300 MHz, as seen in some pulsars in group A such as B0138+59 and B0751+32. The pulsar B0943+10 is relatively unique. Although it is classified into Group B, according to [80], B0943+10 exhibits more clear variations in its radio emission at frequencies below 40 MHz. However, we did not obtain data for this pulsar at frequencies below 40 MHz here. Further research awaits the release of more low-frequency data for confirmation.

Furthermore, the majority of pulsars in Group B exhibit relatively low emission altitudes. We tend to express the phenomenon observed in Group B pulsars as follows: pulsars with relatively constant emission beam radii across different frequencies tend to have their emission regions located closer to the pulsar surface compared to those that conform to the RFM. In Group B, B1737+30 is an exception, as its emission height exceeds 500 km across the currently known frequency range (920 MHz to 8.4 GHz), while the average emission altitude of the other seven pulsars is less than 160 km. Its emission altitude is significantly higher than that of the other pulsars. However, it is worth noting that we lack

observations of this pulsar at lower frequencies, making it difficult to determine whether its emission altitude would suddenly increase at even lower frequencies, just like in pulsars from group A. Low-frequency observations might alter the results, but at least within the frequency range of our current study, its emission altitude remains almost unchanged.

4.3. Group C

Compared to the first two groups of pulsars, the emission altitude of pulsars in group C increases with frequency, showing an opposite evolution behavior. In other words, low-frequency emissions originate from an emission zone close to the neutron star's surface, while high-frequency emissions come from a zone that is farther from the pulsar's surface. This phenomenon is difficult to explain using the traditional RFM model. There are relatively few pulsars in this group, with only eight pulsars in our statistical sample, as shown in Figure 4. Although the frequency range we studied is not as broad compared to the first two groups of pulsars, the opposite evolution behavior of emission altitude is evident within the frequency range we provided. The evolutionary trend of these pulsars that contradicts the RFM model may indicate that they possess unique emission beam structures. The traditional narrowband interpretation based on the RS model struggles to account for such pulsars. Perhaps this necessitates an alternative narrowband model, namely the ICS model. This will be discussed in detail in Section 5.

4.4. Statistical Analysis of Emission Altitude Characteristics

We estimated the distribution of emission altitudes for pulsars in different groups at 40, 100, 400, and 4850 MHz, with the results shown in Figure 5. It can be seen that the emission altitudes of pulsars in Group A are concentrated around 250 km at 4850 MHz. At 400 MHz, the emission altitudes increase, but most remain within the range of less than 500 km. By 100 MHz, the emission altitudes of the majority of Group A pulsars show a significant increase, and at 40 MHz, half of the pulsars in Group A have emission altitudes exceeding 500 km. The emission altitudes of pulsars in Group B remain largely unchanged across the four frequency bands. In most cases, their emission altitudes are lower than those of pulsars in Group A. With the exception of pulsar B1737−30, the emission altitudes of the remaining pulsars in Group B are all below 250 km. In contrast to Group A pulsars, those in Group C show little overall change in emission altitude from 40 MHz to 400 MHz, with the emission regions concentrated below 250 km. At 4850 MHz, the emission altitudes of most pulsars in Group C exceed 250 km, with one pulsar reaching up to 500 km.

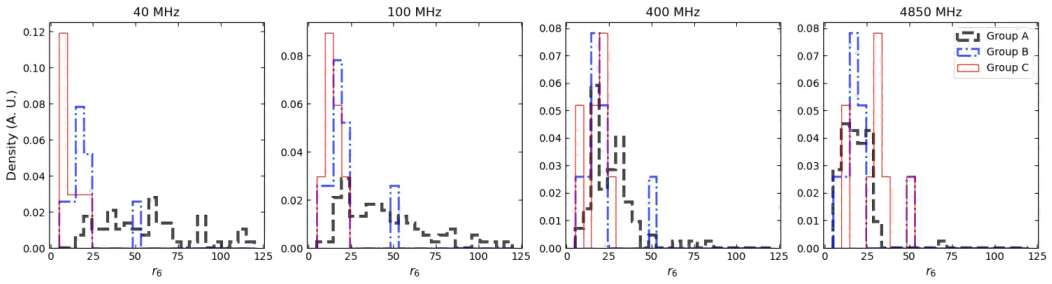

Figure 5. The graph illustrates the probability distribution of the index n for pulsar groups A, B, and C. The horizontal axis represents the emission altitude, scaled in units of 10 km, while the vertical axis indicates the probability.

Table 2. Parameters for 104 Pulsars. Pulsar Jnames and Bnames are listed in columns (1) and (2). Columns (3)–(12) give the period, frequency range, and least-square fitting scaling coefficients A, n, and C, along with their 95% confidence intervals and the minimized chi-square value, number of data points, inclination angle α, and impact angle β. The 12th column provides the references for magnetic inclination and impact angle: TO22: Olszanski, Timothy [35]; RK22: Rankin, Joanna [34]; RK93: Rankin, Joanna M [73]; RK83: Rankin, J.M [11]; LM88: Lyne and Manchester [12]; WHG14: Wang, H.G [6].

Bname	Jname	P s	Bands (GHz)	A	n	C	$\chi^2_{\min}$	N	α °	β °	Reference
B0031−07	J0034−0721	0.943	0.038–4.85	$3.30 \times 10^{4+2.27\times10^{3}}_{-2.27\times10^{3}}$	$-1.32^{+0.02}_{-0.02}$	$264.48^{+0.75}_{-0.75}$	7.69	19	6.0	6.0	RK22
B0052+51	J0055+5117	2.120	0.129–4.85	$3.08 \times 10^{4+1.27\times10^{3}}_{-1.27\times10^{3}}$	$-0.78^{+0.01}_{-0.01}$	$235.71^{+2.91}_{-2.91}$	9.95	7	50.0	0.0	RK22
B0105+65	J0108+6608	1.280	0.129–1.4	$9.99 \times 10^{7+5.56\times10^{7}}_{-9.99\times10^{7}}$	$-2.64^{+0.71}_{-0.71}$	$162.38^{+1.4}_{-1.4}$	0.1	5	18.0	3.5	RK22
B0136+57	J0139+5814	0.272	0.23–4.75	$9.99 \times 10^{7+7.19\times10^{7}}_{-9.99\times10^{7}}$	$-2.28^{+0.33}_{-0.33}$	$113.54^{+1.13}_{-1.13}$	1.29	8	42.0	−7.3	RK22
B0138+59	J0141+6009	1.223	0.04–4.85	$7.29 \times 10^{4+5.29\times10^{3}}_{-5.29\times10^{3}}$	$-1.42^{+0.02}_{-0.02}$	$283.66^{+0.9}_{-0.9}$	29.39	10	20.0	2.2	RK22
B0149−16	J0152−1637	0.833	0.035–3.1	$3.59 \times 10^{4+4.19\times10^{3}}_{-4.19\times10^{3}}$	$-1.42^{+0.03}_{-0.03}$	$175.62^{+0.86}_{-0.86}$	67.31	11	84.0	1.9	RK22
B0254−53	J0255−5304	0.448	0.434–1.56	$4.24 \times 10^{2+5.01\times10^{2}}_{-4.24\times10^{2}}$	$-0.23^{+0.52}_{-0.52}$	$0^{+96.01}_{-0.0}$	2.56	5	90.0	2.9	RM88
B0301+19	J0304+1932	1.388	0.129-4.6	$5.96 \times 10^{3+3.12\times10^{2}}_{-3.12\times10^{2}}$	$-0.54^{+0.01}_{-0.01}$	$163.07^{+4.83}_{-4.83}$	3.65	9	40.0	2.2	TO22
B0331+45	J0335+4555	0.269	0.15–1.5	$6.23 \times 10^{2+3.79\times10^{2}}_{-3.79\times10^{2}}$	$-0.46^{+0.16}_{-0.16}$	$102.46^{+12.14}_{-12.14}$	1.13	7	33.0	7.8	RK22
B0402+61	J0406+6138	0.595	0.15–4.85	$9.89 \times 10^{7+8.80\times10^{7}}_{-9.89\times10^{7}}$	$-1.99^{+0.02}_{-0.02}$	$277.97^{+1.06}_{-1.06}$	67.47	9	83.0	2.2	RK22
B0410+69	J0415+6954	0.391	0.15–1.5	$3.07 \times 10^{6+1.51\times10^{6}}_{-1.51\times10^{6}}$	$-1.99^{+0.1}_{-0.1}$	$132.97^{+1.45}_{-1.45}$	3.06	7	64.0	5.7	RK22
B0450+55	J0454+5543	0.341	0.04–4.82	$1.10 \times 10^{4+4.21\times10^{3}}_{-4.21\times10^{3}}$	$-1.36^{+0.1}_{-0.1}$	$151.32^{+1.17}_{-1.17}$	3.65	7	28.0	3.0	RK22
B0450−18	J0452−1759	0.549	0.333–4.85	$1.06 \times 10^{2+6.69\times10^{1}}_{-1.06\times10^{2}}$	$0.01^{+2.2}_{-2.02}$	$53.32^{+132.88}_{-53.32}$	2.06	7	24.0	4.0	RK22
B0458+46	J0502+4654	0.639	0.408–4.85	$9.78 \times 10^{7+8.07\times10^{7}}_{-9.78\times10^{7}}$	$-1.92^{+0.12}_{-0.12}$	$122.58^{+1.8}_{-1.8}$	1.71	7	31.0	4.2	RK22
B0523+11	J0525+1115	0.354	0.327–4.6	$1.49 \times 10^{3+3.70\times10^{2}}_{-3.70\times10^{2}}$	$-0.40^{+0.06}_{-0.06}$	$182.79^{+14.41}_{-14.41}$	7.88	8	83.0	−6.0	TO22
B0525+21	J0528+2200	3.746	0.04–4.82	$1.52 \times 10^{3+1.50\times10^{1}}_{-1.50\times10^{1}}$	$-0.23^{+0.01}_{-0.01}$	$0^{+9.65}_{-0.0}$	34.99	14	21.0	0.6	TO22
B0540+23	J0543+2329	0.246	0.23–10.55	$8.64 \times 10^{6+9.25\times10^{6}}_{-8.64\times10^{6}}$	$-2.22^{+0.2}_{-0.2}$	$228.80^{+0.66}_{-0.66}$	2.31	17	38.0	−10.0	TO22
B0559−05	J0601−0527	0.396	0.4–4.85	$3.51 \times 10^{4+1.38\times10^{4}}_{-1.38\times10^{4}}$	$-0.97^{+0.07}_{-0.07}$	$177.22^{+3.08}_{-3.08}$	7.61	9	51.8	1.8	RK22
B0609+37	J0612+3721	0.298	0.15–4.85	$1.30 \times 10^{4+1.92\times10^{3}}_{-1.92\times10^{3}}$	$-0.86^{+0.03}_{-0.03}$	$94.91^{+2.02}_{-2.02}$	52.37	10	50.0	1.8	TO22
B0611+22	J0614+2229	0.335	0.333–4.85	$9.01 \times 10^{1+5.96\times10^{1}}_{-9.01\times10^{1}}$	$-0.02^{+1.46}_{-1.62}$	$75.18^{+89.78}_{-75.18}$	1.21	7	35.0	6.7	TO22
B0626+24	J0629+2415	0.477	0.129–4.85	$9.85 \times 10^{7+8.48\times10^{7}}_{-9.23\times10^{7}}$	$-2.27^{+0.08}_{-0.08}$	$253.12^{+1.0}_{-1.0}$	37.76	9	63.0	4.3	TO22
B0628−28	J0630−2834	1.244	0.035–10.55	$1.22 \times 10^{4+1.38\times10^{3}}_{-1.38\times10^{3}}$	$-1.21^{+0.03}_{-0.03}$	$185.51^{+0.72}_{-0.72}$	50.27	17	14.0	−3.3	RK22
B0656+14	J0659+1414	0.385	0.149–6.2	$1.41 \times 10^{4+2.00\times10^{3}}_{-2.00\times10^{3}}$	$-0.90^{+0.03}_{-0.03}$	$109.82^{+1.5}_{-1.5}$	8.08	14	19.0	4.7	TO22
B0727−18	J0729−1836	0.510	0.333–1.6	$5.09 \times 10^{3+2.50\times10^{3}}_{-2.50\times10^{3}}$	$-0.57^{+0.1}_{-0.1}$	$226.23^{+21.85}_{-21.85}$	5.05	6	70.0	4.5	RK22
B0736−40	J0738−4042	0.375	0.674–8.6	$7.69 \times 10^{3+4.30\times10^{3}}_{-4.30\times10^{3}}$	$-0.69^{+0.09}_{-0.09}$	$79.71^{+5.51}_{-5.51}$	0.54	9	17.0	4.3	RK93
B0740−28	J0742−2822	0.167	0.333–10.55	$5.75 \times 10^{3+5.14\times10^{3}}_{-5.14\times10^{3}}$	$-0.90^{+0.16}_{-0.16}$	$134^{+1.94}_{-1.94}$	1.06	13	37.0	9.9	RK22
B0751+32	J0754+3231	1.442	0.102–4.85	$9.86 \times 10^{7+8.80\times10^{7}}_{-8.91\times10^{7}}$	$-2.04^{+0.01}_{-0.01}$	$257.40^{+0.95}_{-0.95}$	44.44	9	26.0	1.0	TO22
B0809+74	J0814+7429	1.292	0.064–10.55	$3.26 \times 10^{6+9.54\times10^{5}}_{-9.54\times10^{5}}$	$-2.41^{+0.07}_{-0.07}$	$227.02^{+0.67}_{-0.67}$	3.69	14	9.0	4.5	RK22
B0818−13	J0820−1350	1.238	0.059–4.82	$9.32 \times 10^{1+3.13\times10^{0}}_{-9.32\times10^{1}}$	$-0.01^{+0.5}_{-0.68}$	$17.89^{+96.86}_{-17.84}$	0.39	9	15.5	3.2	RK22
B0820+02	J0823+0159	0.865	0.135–1.5	$4.45 \times 10^{5+4.17\times10^{4}}_{-4.17\times10^{4}}$	$-1.42^{+0.02}_{-0.02}$	$325.58^{+1.67}_{-1.67}$	18.19	8	71.0	4.5	RK93
B0823+26	J0826+2637	0.531	0.038–10.55	$4.28 \times 10^{4+7.41\times10^{2}}_{-7.41\times10^{2}}$	$-1.06^{+0.0}_{-0.0}$	$48.08^{+0.89}_{-0.89}$	277.21	15	84.0	3.3	TO22
B0834+06	J0837+0610	1.274	0.035–4.6	$1.24 \times 10^{5+8.83\times10^{3}}_{-8.83\times10^{3}}$	$-1.65^{+0.02}_{-0.02}$	$160.32^{+0.77}_{-0.77}$	34.18	13	50.0	2.6	TO22
B0844−35	J0846−3533	1.116	0.315–1.44	$2.98 \times 10^{3+1.24\times10^{3}}_{-1.24\times10^{3}}$	$-0.45^{+0.09}_{-0.1}$	$0^{+34.66}_{-0.0}$	1.59	7	19.0	0.7	RK22
B0906−17	J0908−1739	0.402	0.078–4.85	$9.02 \times 10^{6+7.23\times10^{7}}_{-9.02\times10^{6}}$	$-3.09^{+1.84}_{-1.84}$	$56.50^{+0.82}_{-0.82}$	0.01	9	9.0	−4.5	RK22
B0917+63	J0921+6254	1.568	0.04–1.5	$1.18 \times 10^{3+4.16\times10^{2}}_{-4.16\times10^{2}}$	$-0.81^{+0.1}_{-0.1}$	$220.88^{+2.36}_{-2.36}$	0.16	8	13.5	4.5	RK22
B0919+06	J0922+0638	0.431	0.103–10.55	$1.83 \times 10^{3+6.69\times10^{1}}_{-6.69\times10^{1}}$	$-0.36^{+0.01}_{-0.01}$	$103^{+4.59}_{-4.59}$	11.32	16	53.0	7.6	TO22
B0940−55	J0942−5552	0.664	0.631–3.1	$3.57 \times 10^{1+4.12\times10^{1}}_{-2.68\times10^{1}}$	$0.26^{+0.11}_{-0.11}$	$0^{+99.99}_{-0.0}$	4.04	4	19.6	5.5	RM88
B0942−13	J0944−1354	0.570	0.23–4.85	$1.03 \times 10^{1+1.37\times10^{2}}_{-1.03\times10^{1}}$	$-0.08^{+0.08}_{-0.0}$	$141.05^{+5.4}_{-141.05}$	0.27	4	55.0	5.2	RK22

Table 2. *Cont.*

Bname	Jname	P s	Bands (GHz)	A	n	C	$\chi^2_{\rm min}$	N	α °	β °	Reference
B0943+10	J0946+0951	1.098	0.04–1.5	$2.18 \times 10^{2}{}^{+1.30\times10^{2}}_{-1.75\times10^{2}}$	$-0.02^{+0.11}_{-0.3}$	$30.32^{+176.0}_{-30.32}$	0.27	7	11.5	−5.4	TO22
B0950+08	J0953+0755	0.253	0.035–10.55	$7.12 \times 10^{3}{}^{+1.85\times10^{3}}_{-1.85\times10^{3}}$	$-1.17^{+0.07}_{-0.07}$	$146.13^{+0.7}_{-0.7}$	1.93	15	12.0	8.5	RK83a
B1039−19	J1041−1942	1.386	0.4–4.85	$9.63 \times 10^{2}{}^{+1.16\times10^{2}}_{-1.16\times10^{2}}$	$-0.20^{+0.03}_{-0.05}$	$0^{+57.12}_{-0.0}$	7.43	7	31.0	1.7	RK22
B1112+50	J1115+5030	1.656	0.04–1.642	$3.38 \times 10^{3}{}^{+1.56\times10^{3}}_{-1.56\times10^{3}}$	$-1.06^{+0.13}_{-0.13}$	$153.39^{+1.87}_{-1.87}$	6.16	6	34.0	2.9	RK22
B1133+16	J1136+1551	1.188	0.035–10.55	$1.38 \times 10^{4}{}^{+4.15\times10^{2}}_{-4.15\times10^{2}}$	$-0.92^{+0.01}_{-0.01}$	$214.29^{+0.88}_{-0.88}$	17.79	15	46.0	4.1	RK93
B1237+25	J1239+2453	1.382	0.04–4.82	$4.61 \times 10^{3}{}^{+1.20\times10^{2}}_{-1.20\times10^{2}}$	$-0.60^{+0.01}_{-0.01}$	$213.74^{+1.94}_{-1.94}$	8.85	11	53.0	−0.3	RK93
B1325−43	J1328−4357	0.533	0.435–1.56	$1.08 \times 10^{3}{}^{+1.21\times10^{3}}_{-7.58\times10^{2}}$	$-0.31^{+0.18}_{-0.33}$	$0^{+110.41}_{-0.0}$	0.15	5	55.0	3.0	WHG14
B1451−68	J1456−6843	0.263	0.045–8.356	$2.91 \times 10^{3}{}^{+5.66\times10^{2}}_{-5.66\times10^{2}}$	$-0.45^{+0.04}_{-0.04}$	$5.69^{+8.99}_{-5.69}$	20.94	7	23.5	3.3	RM88
B1508+55	J1509+5531	0.740	0.059–4.82	$9.84 \times 10^{7}{}^{+7.99\times10^{7}}_{-1.85\times10^{7}}$	$-2.93^{+0.21}_{-0.21}$	$127.72^{+0.87}_{-0.87}$	2.49	9	45.0	−2.7	RK22
B1530+27	J1532+2745	1.125	0.103–4.6	$6.21 \times 10^{4}{}^{+8.89\times10^{3}}_{-8.89\times10^{3}}$	$-1.24^{+0.03}_{-0.03}$	$242.48^{+1.28}_{-1.28}$	4.35	11	30.0	4.9	TO22
B1540−06	J1543−0620	0.709	0.04–4.75	$2.80 \times 10^{3}{}^{+3.77\times10^{2}}_{-3.77\times10^{2}}$	$-0.81^{+0.04}_{-0.04}$	$142.38^{+1.68}_{-1.68}$	8.91	9	38.0	5.0	RK22
B1556−44	J1559−4438	0.257	0.333–4.82	$6.12 \times 10^{0}{}^{+4.64\times10^{0}}_{-3.70\times10^{0}}$	$0.36^{+0.07}_{-0.07}$	$0.43^{+17.56}_{-0.43}$	7.42	7	32.0	2.4	RK93
B1604−00	J1607−0032	0.422	0.035–4.85	$7.58 \times 10^{4}{}^{+1.74\times10^{3}}_{-1.74\times10^{3}}$	$-1.26^{+0.01}_{-0.01}$	$140.39^{+0.96}_{-0.96}$	131.84	12	48.0	5.3	TO22
B1612+07	J1614+0737	1.207	0.035–4.6	$2.07 \times 10^{2}{}^{+8.42\times10^{1}}_{-2.07\times10^{2}}$	$-0.01^{+0.22}_{-0.22}$	$36.78^{+198.83}_{-36.78}$	1.68	9	24.0	5.1	TO22
B1633+24	J1635+2418	0.491	0.04–1.4	$4.05 \times 10^{1}{}^{+3.22\times10^{1}}_{-3.03\times10^{1}}$	$0.23^{+0.1}_{-0.09}$	$0^{+76.23}_{-0.0}$	0.85	4	19.0	−4.8	RK93
B1649−23	J1652−2404	1.704	0.4–4.85	$2.68 \times 10^{3}{}^{+3.40\times10^{3}}_{-2.68\times10^{3}}$	$-0.72^{+0.23}_{-0.23}$	$687.81^{+5.87}_{-5.87}$	0.03	6	90.0	5.7	RM88
B1700−32	J1703−3241	1.212	0.05–1.369	$1.83 \times 10^{5}{}^{+9.72\times10^{4}}_{-9.72\times10^{4}}$	$-1.19^{+0.1}_{-0.1}$	$219.03^{+6.84}_{-6.84}$	0.19	5	48.0	1.8	RK93
B1706−16	J1709−1640	0.650	0.05–10.55	$9.86 \times 10^{7}{}^{+8.62\times10^{7}}_{-9.11\times10^{7}}$	$-2.79^{+0.07}_{-0.07}$	$156.34^{+0.58}_{-0.58}$	34.94	16	49.0	−4.8	RK93
B1706−44	J1709−4429	0.102	0.45–8.6	$3.62 \times 10^{6}{}^{+5.85\times10^{5}}_{-5.85\times10^{5}}$	$-1.49^{+0.03}_{-0.03}$	$189.64^{+1.83}_{-1.83}$	0.77	5	38.1	12.9	WHG14
B1717−29	J1720−2933	0.620	0.333–4.85	$2.12 \times 10^{3}{}^{+2.51\times10^{2}}_{-2.51\times10^{2}}$	$-0.32^{+0.03}_{-0.03}$	$0^{+21.83}_{-0.0}$	21.13	7	34.6	4.7	RK22
B1718−32	J1722−3207	0.477	0.4–1.642	$9.86 \times 10^{7}{}^{+7.89\times10^{7}}_{-9.59\times10^{7}}$	$-1.92^{+0.17}_{-0.17}$	$72.14^{+2.86}_{-2.86}$	4.74	6	39.0	2.4	RK22
B1737−30	J1740−3015	0.607	0.408–8.356	$0.00 \times 10^{0}{}^{+5.24\times10^{2}}_{-0.00\times10^{0}}$	$0^{+0.0}_{-0.87}$	$511.69^{+26.2}_{-51.6}$	0.34	6	58.0	10.9	RK22
B1738−08	J1741−0840	2.043	0.4–4.85	$1.46 \times 10^{3}{}^{+1.84\times10^{2}}_{-1.84\times10^{2}}$	$-0.25^{+0.03}_{-0.04}$	$0^{+39.75}_{-0.0}$	6.24	6	26.0	1.7	RK22
B1749−28	J1752−2806	0.563	0.149–8.6	$9.59 \times 10^{7}{}^{+4.71\times10^{7}}_{-9.50\times10^{7}}$	$-2.55^{+0.74}_{-0.78}$	$64.68^{+0.93}_{-0.93}$	14.02	8	42.0	2.9	RK22
B1804−08	J1807−0847	0.164	0.4–8.6	$9.76 \times 10^{7}{}^{+8.43\times10^{7}}_{-9.09\times10^{7}}$	$-1.84^{+0.06}_{-0.06}$	$154.93^{+1.27}_{-1.27}$	28.82	8	69.0	3.1	RK22
B1819−22	J1822−2256	1.874	0.333–4.85	$9.88 \times 10^{7}{}^{+8.16\times10^{7}}_{-9.60\times10^{7}}$	$-1.97^{+0.13}_{-0.13}$	$264.23^{+1.65}_{-1.65}$	0.43	6	16.0	4.0	RK22
B1826−17	J1829−1751	0.307	0.66–8.6	$1.94 \times 10^{5}{}^{+9.12\times10^{4}}_{-9.12\times10^{4}}$	$-1.15^{+0.07}_{-0.07}$	$56.66^{+2.44}_{-2.44}$	3.92	6	39.6	0.7	RM88
B1831−04	J1834−0426	0.290	0.103–4.85	$7.55 \times 10^{1}{}^{+4.68\times10^{1}}_{-4.31\times10^{1}}$	$0.13^{+0.04}_{-0.05}$	$83.42^{+59.0}_{-59.01}$	2.72	9	10.0	2.0	RK22
B1839+09	J1841+0912	0.381	0.129–4.85	$9.79 \times 10^{7}{}^{+7.71\times10^{7}}_{-9.60\times10^{7}}$	$-2.38^{+0.23}_{-0.23}$	$138.39^{+0.83}_{-0.83}$	8.67	10	83.0	3.0	TO22
B1839+56	J1840+5640	1.653	0.065–4.85	$7.67 \times 10^{1}{}^{+1.58\times10^{1}}_{-1.61\times10^{1}}$	$0.18^{+0.02}_{-0.02}$	$0^{+23.39}_{-0.0}$	30.59	8	40.0	3.0	RK22
B1845−01	J1848−0123	0.659	0.618–10.55	$9.82 \times 10^{7}{}^{+8.63\times10^{7}}_{-9.02\times10^{7}}$	$-1.66^{+0.03}_{-0.03}$	$267.85^{+1.19}_{-1.19}$	66.99	10	39.0	4.5	RK22
B1848+12	JJ1851+1259	1.205	0.129–4.6	$4.17 \times 10^{6}{}^{+1.38\times10^{6}}_{-1.38\times10^{6}}$	$-2.01^{+0.07}_{-0.07}$	$61.44^{+1.26}_{-1.26}$	5.95	6	63.0	1.4	TO22
B1905+39	J1907+4002	1.236	0.102–4.85	$9.86 \times 10^{7}{}^{+8.74\times10^{7}}_{-8.97\times10^{7}}$	$-2.15^{+0.03}_{-0.03}$	$302.21^{+0.95}_{-0.95}$	50.2	8	33.0	2.1	RK22
B1911−04	J1913−0440	0.826	0.333–4.85	$3.12 \times 10^{1}{}^{+5.07\times10^{1}}_{-3.00\times10^{1}}$	$0.14^{+0.2}_{-0.13}$	$0^{+82.12}_{-0.0}$	5.16	6	64.0	−1.9	RK22
B1913+167	J1915+1647	1.616	0.4–1.4	$5.84 \times 10^{3}{}^{+2.77\times10^{3}}_{-2.77\times10^{3}}$	$-0.46^{+0.1}_{-0.11}$	$0^{+62.24}_{-0.0}$	3.83	4	53.9	1.8	RM88
B1914+09	J1916+0951	0.270	0.143–4.85	$6.92 \times 10^{6}{}^{+7.17\times10^{6}}_{-5.50\times10^{6}}$	$-2.23^{+0.21}_{-0.21}$	$150.35^{+1.05}_{-1.05}$	8.09	8	52.0	−6.5	TO22
B1916+14	J1918+1444	1.181	0.327–4.6	$1.06 \times 10^{3}{}^{+2.16\times10^{2}}_{-2.16\times10^{2}}$	$-0.30^{+0.05}_{-0.06}$	$0^{+25.81}_{-0.0}$	4.67	6	79.0	1.2	WHG14
B1918+19	J1921+1948	0.821	0.4–1.6	$5.56 \times 10^{1}{}^{+6.66\times10^{1}}_{-5.03\times10^{1}}$	$0.21^{+0.19}_{-0.12}$	$0^{+170.04}_{-0.0}$	4.52	4	14.0	0.9	RM88
B1919+21	J1921+2153	1.337	0.038–4.6	$1.00 \times 10^{7}{}^{+1.86\times10^{6}}_{-1.86\times10^{6}}$	$-2.96^{+0.05}_{-0.05}$	$249.94^{+0.83}_{-0.83}$	11.33	10	45.0	−3.7	TO22
B1920+21	J1922+2110	1.078	0.35–1.642	$2.29 \times 10^{1}{}^{+2.06\times10^{1}}_{-1.43\times10^{1}}$	$0.36^{+0.1}_{-0.09}$	$0^{+66.35}_{-0.0}$	4.4	5	47.2	1.2	RM88
B1923+04	J1926+0431	1.074	0.135–4.85	$4.39 \times 10^{4}{}^{+3.55\times10^{4}}_{-3.55\times10^{4}}$	$-1.36^{+0.17}_{-0.17}$	$137.49^{+1.48}_{-1.48}$	0.17	8	25.0	4.0	TO22
B1924+16	J1926+1648	0.580	0.327–4.6	$9.96 \times 10^{6}{}^{+2.70\times10^{7}}_{-9.96\times10^{6}}$	$-2.18^{+0.47}_{-0.47}$	$149.43^{+1.47}_{-1.47}$	5.54	7	34.0	5.0	RK93
B1929+10	J1932+1059	0.227	0.065–10.55	$1.67 \times 10^{3}{}^{+9.96\times10^{1}}_{-9.96\times10^{1}}$	$-0.38^{+0.01}_{-0.01}$	$191.90^{+4.26}_{-4.26}$	14.45	16	88.0	10.5	TO22
B1935+25	J1937+2544	0.201	0.327–4.92	$5.79 \times 10^{3}{}^{+6.67\times10^{2}}_{-6.67\times10^{2}}$	$-0.52^{+0.02}_{-0.02}$	$255.46^{+7.11}_{-7.11}$	9.86	8	77.0	6.2	TO22

Table 2. *Cont.*

Bname	Jname	P s	Bands (GHz)	A	n	C	χ^2_{min}	N	α °	β °	Reference
B1952+29	J1954+2923	0.427	0.102–4.92	$1.44 \times 10^{3}{}^{+4.17\times10^{1}}_{-4.17\times10^{1}}$	$-0.24^{+0.01}_{-0.01}$	$0^{+17.41}_{-0.0}$	13.41	7	43.0	−1.0	TO22
B1953+50	J1955+5059	0.519	0.04–4.92	$7.07 \times 10^{2}{}^{+7.65\times10^{1}}_{-7.65\times10^{1}}$	$-0.47^{+0.04}_{-0.04}$	$146.77^{+3.95}_{-3.95}$	0.5	8	90.0	5.7	RK22
B2003−08	J2006−0807	0.581	0.4–1.4	$3.78 \times 10^{5}{}^{+8.67\times10^{5}}_{-3.65\times10^{5}}$	$-1.49^{+0.4}_{-0.39}$	$244.72^{+6.06}_{-6.06}$	0.0	4	13.0	3.3	RK22
B2016+28	J2018+2839	0.558	0.065–10.55	$2.31 \times 10^{5}{}^{+3.84\times10^{4}}_{-3.84\times10^{4}}$	$-1.76^{+0.04}_{-0.04}$	$279.71^{+0.71}_{-0.71}$	2.42	13	39.0	7.2	TO22
B2020+28	J2022+2854	0.343	0.059–10.55	$9.67 \times 10^{3}{}^{+5.98\times10^{2}}_{-5.98\times10^{2}}$	$-0.71^{+0.01}_{-0.01}$	$201.77^{+1.97}_{-1.97}$	25.53	11	80.0	7.2	TO22
B2021+51	J2022+5154	0.529	0.12–10.55	$1.60 \times 10^{3}{}^{+2.59\times10^{2}}_{-2.59\times10^{2}}$	$-0.58^{+0.04}_{-0.04}$	$128.83^{+2.17}_{-2.17}$	1.28	13	23.0	5.6	RK22
B2044+15	J2046+1540	1.138	0.129–1.5	$2.70 \times 10^{3}{}^{+4.09\times10^{2}}_{-4.09\times10^{2}}$	$-0.50^{+0.04}_{-0.04}$	$184.96^{+10.57}_{-10.57}$	2.27	7	40.0	3.4	RK93
B2045−16	J2048−1616	1.962	0.102–10.55	$3.66 \times 10^{4}{}^{+1.79\times10^{3}}_{-1.79\times10^{3}}$	$-0.94^{+0.01}_{-0.01}$	$194.14^{+1.12}_{-1.12}$	17.98	13	34.0	−1.2	RK22
B2106+44	J2108+4441	0.415	0.35–4.75	$1.00 \times 10^{7}{}^{+1.35\times10^{7}}_{-1.00\times10^{7}}$	$-2.06^{+0.23}_{-0.23}$	$149.16^{+1.63}_{-1.63}$	1.64	6	11.5	6.4	RK22
B2110+27	J2113+2754	1.203	0.035–4.85	$3.50 \times 10^{6}{}^{+3.02\times10^{5}}_{-3.02\times10^{5}}$	$-2.50^{+0.02}_{-0.02}$	$165.16^{+0.69}_{-0.69}$	21.45	13	48.0	3.9	TO22
B2111+46	J2113+4644	1.015	0.151–4.85	$9.86 \times 10^{6}{}^{+1.10\times10^{7}}_{-9.86\times10^{6}}$	$-2.29^{+0.22}_{-0.22}$	$241.79^{+1.17}_{-1.17}$	51.74	7	9.0	1.4	RK22
B2148+63	J2149+6329	0.380	0.35–4.85	$1.98 \times 10^{4}{}^{+4.25\times10^{4}}_{-1.98\times10^{4}}$	$-1.15^{+0.38}_{-0.38}$	$130.71^{+2.82}_{-2.82}$	0.04	6	10.5	7.0	RK22
B2152−31	J2155−3118	1.030	0.23–1.56	$4.07 \times 10^{2}{}^{+2.34\times10^{2}}_{-2.34\times10^{2}}$	$-0.25^{+0.24}_{-0.24}$	$73.60^{+75.66}_{-73.6}$	0.17	5	32.0	3.4	RK22
B2154+40	J2157+4017	1.525	0.102–4.85	$1.54 \times 10^{6}{}^{+2.17\times10^{5}}_{-2.17\times10^{5}}$	$-1.84^{+0.03}_{-0.03}$	$263.74^{+1.03}_{-1.03}$	12.68	9	20.0	2.5	RK22
B2306+55	J2308+5547	0.475	0.129–4.85	$3.71 \times 10^{3}{}^{+3.18\times10^{2}}_{-3.18\times10^{2}}$	$-0.54^{+0.02}_{-0.02}$	$225.59^{+4.95}_{-4.95}$	16.51	8	54.0	1.9	RK22
B2310+42	J2313+4253	0.349	0.102–10.55	$1.39 \times 10^{4}{}^{+3.02\times10^{3}}_{-3.02\times10^{3}}$	$-1.04^{+0.05}_{-0.05}$	$193.26^{+1.22}_{-1.22}$	3.38	10	56.0	6.8	TO22
B2315+21	J2317+2149	1.445	0.129–4.85	$5.12 \times 10^{2}{}^{+1.02\times10^{2}}_{-1.02\times10^{2}}$	$-0.09^{+0.04}_{-0.04}$	$0^{+131.73}_{-0.0}$	4.23	7	88.0	3.4	RK22
B2319+60	J2321+6024	2.256	0.23–10.55	$1.10 \times 10^{4}{}^{+9.80\times10^{2}}_{-9.80\times10^{2}}$	$-0.68^{+0.02}_{-0.02}$	$183.44^{+2.63}_{-2.63}$	10.2	9	18.0	2.2	RK22
B2323+63	J2325+6316	1.436	0.4–1.6	$6.06 \times 10^{2}{}^{+5.60\times10^{2}}_{-5.60\times10^{2}}$	$-0.10^{+0.17}_{-0.29}$	$0^{+304.08}_{-0.0}$	0.14	5	14.5	2.9	RK22
B2324+60	J2326+6113	0.234	0.408–1.6	$1.65 \times 10^{3}{}^{+8.95\times10^{2}}_{-8.95\times10^{2}}$	$-0.32^{+0.12}_{-0.15}$	$0^{+92.08}_{-0.0}$	4.95	5	29.0	7.3	RK22
B2327−20	J2330−2005	0.529	0.065–4.92	$5.97 \times 10^{1}{}^{+5.07\times10^{1}}_{-5.97\times10^{1}}$	$0.03^{+0.29}_{-0.28}$	$0^{+83.4}_{-0.0}$	3.35	9	60.0	3.3	RK22
B2351+61	J2337+6151	0.945	0.23–10.55	$6.60 \times 10^{2}{}^{+3.35\times10^{1}}_{-3.35\times10^{1}}$	$-0.18^{+0.02}_{-0.03}$	$0^{+31.95}_{-0.0}$	1.21	8	42.0	3.5	RK22

Notes: Download link for full table https://github.com/pulsar-man/A-Study-on-the-Evolution-of-Emission-Altitude-with-Frequency-Among-104-Normal-Pulsars [Github] (accessed on 4 January 2025).

5. Discussion and Conclusions

Using databases from the European Pulsar Network (EPN), the Australia Telescope National Facility (ATNF), and the published literature, we investigated the multifrequency emission altitude of 104 normal pulsars using the method proposed by Gil, J.A. and Kijak, J. [20] to estimate their altitude in the emission region. In this study, we found that the relationship between pulsar emission altitude and frequency follows a power-law function plus a constant ($r_6 = A\nu^n + C$). We classified the pulsars into three groups based on the variation rate of emission altitude (η= $(r_{4850\,\mathrm{MHz}} - r_{40\,\mathrm{MHz}})/r_{40\,\mathrm{MHz}}$). The results led to the following observations.

1. In this study, each pulsar exhibits different power-law indices. Most of the best-fit indices are continuously distributed. The n indices of the sampled pulsars show distinct clustering regions. Specifically, the n indices of Group A are all less than 0, reaching -0.5; the n indices of Group B concentrate near 0; and the n indices of Group C are all positive.

2. The rate of change in emission serves as the criterion for classifying pulsars. We categorize pulsars with $\eta \leq -0.1$ as Group A, with 88 pulsars (85%); pulsars with $\eta \leq 0.1$ and $\eta > -0.1$ as Group B, with 8 pulsars (7.5%); and pulsars with $\eta \geq 0.1$ as Group C, also with 8 pulsars (7.5%).

3. Our results indicate that pulsars with relatively constant emission beam radii across different frequencies tend to have their emission regions located closer to the pulsar surface compared to those that conform to the RFM, especially in the low-frequency band (below 300 MHz).

The statistical results of this study indicate that the phenomenon in which the emission altitude decreases as frequency increases (Group A) is more prevalent than the phenomenon where the emission altitude remains nearly constant across frequencies (Group B) and the phenomenon where the emission altitude increases as frequency increases (Group C). This may partly explain why pulsars conforming to the RFM model have been the focal point of previous research. Note that some of the class B pulsars show an almost constant frequency dependence of their emission altitude in the frequency range of our investigation, e.g., B0450−18 and B1737−30, and if they were observed at lower frequencies, they might show evolutionary behavior similar to B0906−17 and B0950+08 (i.e., they might belong to class A). But for the current frequency range, their radiative elevation does tend to be stabilized, which is validated with the need for more low-frequency observations.

Compared to the grouping in Chen and Wang [29], Group A accounts for a larger proportion in this study, which may be attributed to the following three reasons: (1) The classification criterion adopted in this study is not the rate of pulse width change, but the rate of emission altitude change, potentially making the multifrequency evolution of pulsars more apparent. (2) This study incorporates low-frequency observational data. After excluding low-frequency data affected by scintillation, most pulsars in Group A exhibit rapid changes when the frequency is below 300 MHz. Examples include pulsars such as B0809+74, B1919+21, and B2016−28. (3) Since calculating the emission altitude using the KG method requires the geometric parameters of pulsars, our sample size of pulsars is smaller compared to Chen and Wang [29], which may also have influenced the statistical results. In comparison to the study by KG98, the current research boasts a larger sample size. Furthermore, there is some overlap between the pulsars used in our study and those in KG98. While the evolutionary trends of these overlapping pulsars are consistent with those reported in KG98, we find slight discrepancies in the emission altitude values. These discrepancies may be related to measurement errors in pulse width W and calculation errors in α and β. The statistical results indicate that for pulsars conforming to the RFM model (Group A), the evolution rate of emission altitude becomes very slow at higher frequencies. Therefore, when describing the emission altitude–frequency relationship, we use a relationship formula that combines a power-law function with a constant. The authors of Wu, Xin-Ji [81] calculated the emission altitude at 618 MHz and 1408 MHz for 18 pulsars conforming to the RFM model using KG and found that their average emission altitudes were 290.1 ± 100.06 km, and 236.4 ± 86.4 km. In this study, using the optimal fitting parameters, the average emission altitudes for Group A pulsars at 618 MHz and 1408 MHz were calculated to be 230.9 km and 201.9 km, respectively. It can be observed that our calculated emission altitude exhibits a certain degree of consistency within the error range. It is important to note that in our work, we used this equation solely to describe the dependence of pulsar emission altitude on frequency. This equation, does not provide any physical insight.

It is worth mentioning that emission altitude, as a non-observable quantity, often yields different values when calculated using various methods [82]. Compared to the BCW method, in principle, the emission altitude calculated by BCW tends to be larger than that calculated by KG. This is due to the fact that geometric methods assume that the emission originates from the outermost open field line and that the measured pulse width W_{10} is smaller than the actual pulse width, among other reasons. However, there exists a certain deviation between this statement and the actual research findings [54,83]. For example, Wang, P.F [54] calculated pulsar data at a central frequency of 1250 MHz observed by the FAST telescope for 108 pulsars using both the BCW and KG methods. They found that for 75 pulsars, the two emission altitudes were consistent within the uncertainties. For 26 pulsars, the KG emission altitude was smaller than that of BCW. This demonstrates

a certain degree of rationality between the emission altitudes calculated by the KG and BCW methods. Deviations between actual observations and theoretical predictions arise from various factors, such as underestimating the theoretical width of the open volume and systematically overestimating the impact angle and dipole inclination.

The GRT method differs notably from the KG and BCW methods. While the KG and BCW methods provide the average emission source within a frequency band, the GRT method, based on the core-cone model, calculates emission altitudes for different components separately. As a result, the emission altitudes obtained using the GRT method often differ significantly from those calculated with the KG method. This is the case for PSR B1839+09, B1916+14, and B2111+46 [84]. In particular, for B2111+46 [85], the multifrequency emission altitude of the cone component calculated using the GRT method differs significantly from the KG method results in this study.

Previous studies have found a certain degree of correlation between the emission altitude and period of Group A pulsars [24,78,81]. However, Rankin, J M. [86] argued that this correlation is not significant. Additionally, some research suggests that the emission altitude may be related to other pulsar parameters, such as characteristic age, period derivative, and magnetic field, but these relationships are weaker compared to the one between period and emission altitude [24,87]. We obtained the connection between the different physical pulsar parameters and emission altitude at 100 MHz (calculated from the best-fit result), as shown in Figure 6, to determine if such correlations exist in our sample. The results indicate that there is no clear correlation between the emission altitude and characteristic age, period, period derivative, or magnetic field strength for Groups A, B, and C. Furthermore, the light-cylinder radii (R_{LC}) show a clear positive correlation with period, but no direct relationship with emission altitude. Our results are more in line with Rankin's conclusion [86]. Note that for Group B and Group C pulsars, due to the limited sample size in this study, we hope future research with more public data will provide deeper insights into their relationships.

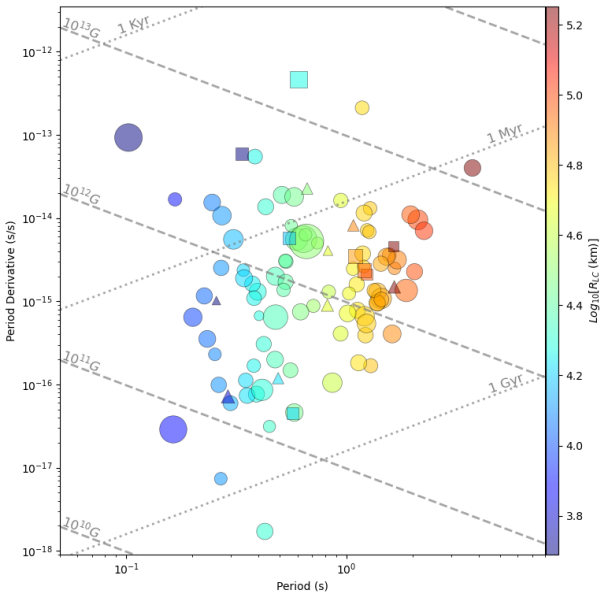

Figure 6. The relationship between emission altitude and various pulsar parameters. The horizontal axis represents the period, and the vertical axis represents the period derivative. The dashed line indicates the magnetic field, while the dotted line represents the characteristic age. Group A is represented by circles, Group B by squares, and Group C by triangles. Different colors correspond to different light-cylinder radii at various heights, and the size of the symbols reflects the relative emission altitude at this frequency.

Regarding the underlying physics of the frequency dependence of emission regions, previous studies have linked the trend of decreasing emission altitude with frequency to the narrowband emission scenario (RFM, [15]). In the narrowband interpretation, the evolution of pulse width with frequency is due to changes in the shape of the emission beam, and these changes in beam shape are caused by the frequency dependence of emission altitude. Specifically, this is understood through the radius-to-frequency mapping based on the RS model [4]. In the RS model, the plasma frequency of secondary particles decreases with increasing altitude because the number density of particles continues to decrease as the plasma flows out; therefore, this decrease leads to the RFM. However, the mechanism excludes the possibility of non-RFM and anti-RFM scenarios and can only explain pulsars in Group A, not those in Group B or C. Mitra and Rankin assumed that a pulsar's emission beam is made up of a core and two hollow cones. Based on their statistical research, they found the following: pulsars with the inner cone component as the main part have a lower emission altitude compared to those dominated by the outer cone component; the frequency evolution of the inner cone is more stable, or behaves oppositely to the outer cone [88]. Therefore, we speculate that pulsars in Group B may be dominated by the inner cone component in their emission. The following is another explanation based on broadband: for pulsars in Group B, the nearly constant emission is attributed to the almost constant pulse width, which is caused by minimal or no spectral variations in the emission region [29]. However, this does not align with our theoretical methods for calculating emission altitude, so we will not discuss it in detail.

The emission altitude of pulsars in Group C increases with frequency, exhibiting evolutionary behavior opposite to that predicted by the RFM. This may indicate that they possess a distinct emission beam structure, which leads to deviations in the lower limit of emission altitude calculated using geometric methods from the actual value. Another narrowband model, the ICS model, may provide an explanation for this phenomenon and offer a method for calculating the emission altitude [17,89,90]. Qiao et al. [5,14] have pointed out that in the ICS model, emission is generated through the ICS process between the low-frequency waves, which are produced in the oscillatory sparking process in the inner vacuum gap, and the secondary relativistic particles. Due to the combination of the highly correlated particle Lorentz factor and particle velocity with the angle of incidence between the low-frequency wave vectors, single-frequency emissions can be generated at three different altitudes along the magnetic field lines. In this way, the entire magnetosphere forms a beam composed of cores, inner cones, and outer cones. The core component of the emission beam does not vary much with frequency, while the emission altitude of the inner cone increases with frequency, and the emission altitude of the outer cone decreases with frequency. Therefore, when the outer cone is too weak and only the inner cone (and/or the core) is visible, the evolutionary phenomenon of pulsars in Group C is observed.

The results above suggest a diversity in the frequency evolution of pulsar emission altitude. Although pulsar groups exhibit similar evolutionary patterns, their n-indices and emission altitude change rates (η) differ, indicating variability in the structure of pulsar emission beams. Existing theoretical models offer valuable insights into certain observed characteristics, but the exploration of pulsar emission mechanisms remains complex. It is worth noting that our sample may have a slight bias due to the lack of low-frequency data for some pulsars, leading to uncertainties in the fitting curves, particularly for PSR B0450−12, B0940−55, and B1737−30. We aim to obtain more low-frequency observations in the future. Nonetheless, even with additional data, pulsars that align with the RFM model will likely remain dominant.

Author Contributions: Methodology, C.L. and Q.Z.; Formal analysls, C.L. and Q.Z.; Data curation C.L., X.X. and C.D.; Project administration, Q.Z.; Methodology, Q.Z.; Investigatlon, Q.Z.; Funding acquisillon, Q.Z.; Supervision, C.D. and Q.Z.; Witing—original draft, C.L.; Writing—review & editing, C.L. and X.X.; Visuallzation, C.L. All authors have read and agreed to the published version of the manuscript.

Funding: This work was supported by the National Natural Science Foundation of China (No.12273008), the National SKA Program of China (Nos. 2022SKA0130100 and 2022SKA0130104), the Natural Science and Technology Foundation of Guizhou Province (No. [2023]024), and the Foundation of Guizhou Provincial Education Department (No. KY(2020)003).

Data Availability Statement: Data is contained within the article.

Conflicts of Interest: The authors declare no conflicts of interest.

References

1. Hewish, A.; Bell, S.J.; Pilkington, J.D.H.; Scott, P.F.; Collins, R.A. Observation of a Rapidly Pulsating Radio Source. *Nature* **1968**, *217*, 709–713. Available online: https://ui.adsabs.harvard.edu/abs/1968Natur.217..709H (accessed on 29 November 2024). [CrossRef]
2. Manchester, R.N.; Hobbs, G.B.; Teoh, A.; Hobbs, M. The Australia Telescope National Facility Pulsar Catalogue. *Astrophys. J.* **2005**, *129*, 1993–2006. Available online: https://ui.adsabs.harvard.edu/abs/2005AJ....129.1993M (accessed on 29 November 2024). [CrossRef]
3. Sturrock, P.A. A Model of Pulsars. *Astrophys. J.* **1971**, *164*, 529. Available online: https://ui.adsabs.harvard.edu/abs/1971ApJ...164..529S (accessed on 29 November 2024). [CrossRef]
4. Ruderman, M.A.; Sutherland, P.G. Theory of Pulsars: Polar Gaps, Sparks, Coherent Microwave Radiation. *Astrophys. J.* **1975**, *196*, 51–72. Available online: https://ui.adsabs.harvard.edu/abs/1975ApJ...196...51R (accessed on 29 November 2024). [CrossRef]
5. Qiao, G.J.; Lin, W.P. An Inverse Compton Scattering (ICS) Model of Pulsar Emission. I. Core and Conal Emission Beams. *Astron. Astrophys.* **1998**, *333*, 172–180. Available online: https://ui.adsabs.harvard.edu/abs/1998A&A...333..172Q (accessed on 29 November 2024).
6. Wang, H.G.; Pi, F.P.; Zheng, X.P.; Deng, C.L.; Wen, S.Q.; Ye, F.; Guan, K.Y.; Liu, Y.; Xu, L.Q. A Fan Beam Model for Radio Pulsars. I. Observational Evidence. *Astrophys. J.* **2014**, *789*, 73. Available online: https://ui.adsabs.harvard.edu/abs/2014ApJ...789...73W (accessed on 29 November 2024). [CrossRef]
7. Goldreich, P.; Julian, W.H. Pulsar Electrodynamics. *Astrophys. J.* **1969**, *157*, 869. Available online: https://ui.adsabs.harvard.edu/abs/1969ApJ...157..869G (accessed on 29 November 2024). [CrossRef]
8. Wang, P.F.; Han, J.L.; Wang, C. Modeling the Frequency Dependence of Radio Beams for Cone-Dominant Pulsars. *Astrophys. J.* **2013**, *768*, 114. Available online: https://ui.adsabs.harvard.edu/abs/2013ApJ...768..114W (accessed on 29 November 2024). [CrossRef]
9. Gil, J.A.; Snakowski, J.K. Curvature Radiation the Core Emission of Pulsars. *Astron. Astrophys.* **1990**, *234*, 237–242. Available online: https://ui.adsabs.harvard.edu/abs/1990A&A...234..237G (accessed on 29 November 2024).
10. Beskin, V.S.; Philippov, A.A. On the Mean Profiles of Radio Pulsars-I. Theory of Propagation Effects. *Mon. Not. R. Astron. Soc.* **2012**, *425*, 814–840. Available online: https://ui.adsabs.harvard.edu/abs/2012MNRAS.425..814B (accessed on 29 November 2024). [CrossRef]
11. Rankin, J.M. Toward an Empirical Theory of Pulsar Emission. I. Morphological Taxonomy. *Astrophys. J.* **1983**, *274*, 333–358. Available online: https://ui.adsabs.harvard.edu/abs/1983ApJ...274..333R (accessed on 29 November 2024). [CrossRef]
12. Lyne, A.G.; Manchester, R.N. The Shape of Pulsar Radio Beams. *Mon. Not. R. Astron. Soc.* **1988**, *234*, 477–508. Available online: https://ui.adsabs.harvard.edu/abs/1988MNRAS.234..477L (accessed on 29 November 2024). [CrossRef]
13. Dyks, J.; Serylak, M.; Os lowski, S.; Saha, L.; Guillemot, L.; Cognard, I.; Rudak, B. A Model for Distortions of Polarisation-Angle Curves in Radio Pulsars. *Astron. Astrophys.* **2016**, *593*, A83. Available online: https://ui.adsabs.harvard.edu/abs/2016A&A...593A..83D (accessed on 29 November 2024). [CrossRef]
14. Qiao, G.J.; Liu, J.F.; Zhang, B.; Han, J.L. An Inverse Compton Scattering (ICS) Model of Pulsar Emission. II. Frequency Behavior of Pulse Profiles. *Astron. Astrophys.* **2001**, *377*, 964–971. Available online: https://ui.adsabs.harvard.edu/abs/2001A&A...377..964Q (accessed on 29 November 2024). [CrossRef]
15. Cordes, J.M. Observational Limits on the Location of Pulsar Emission Regions. *Astrophys. J.* **1978**, *222*, 1006–1011. Available online: https://ui.adsabs.harvard.edu/abs/1978ApJ...222.1006C (accessed on 29 November 2024). [CrossRef]
16. Kijak, J.; Gil, J. Radio Emission Regions in Pulsars. *Mon. Not. R. Astron. Soc.* **1998**, *299*, 855–861. Available online: https://ui.adsabs.harvard.edu/abs/1998MNRAS.299..855K (accessed on 29 November 2024). [CrossRef]

17. Zhang, H.; Qiao, G.J.; Han, J.L.; Lee, K.J.; Wang, H.G. PSR B2111+46: A Test of the Inverse Compton Scattering Model of Radio Emission. *Astron. Astrophys.* **2007**, *465*, 525–531. Available online: https://ui.adsabs.harvard.edu/abs/2007A&A...465..525Z (accessed on 29 November 2024). [CrossRef]
18. Gangadhara, R.T. On The Method Of Estimating Emission Altitude from Relativistic Phase Shift in Pulsars. *Astrophys. J.* **2005**, *628*, 923–930. Available online: https://ui.adsabs.harvard.edu/abs/2005ApJ...628..923G (accessed on 29 November 2024). [CrossRef]
19. Gwinn, C.R.; Ojeda, M.J.; Britton, M.C.; Reynolds, J.E.; Jauncey, D.L.; King, E.A.; McCulloch, P.M.; Lovell, J.E.J.; Flanagan, C.S.; Smits, D.P.; Preston, R.A.; Jones, D.L. Size of the VELA Pulsar's Radio Emission Region: 500 Kilometers. *Astrophys. J. Lett.* **1997**, *483*, L53–L56. Available online: https://ui.adsabs.harvard.edu/abs/1997ApJ...483L..53G (accessed on 29 November 2024). [CrossRef]
20. Gil, J.A.; Kijak, J. Period Dependence of Radio Emission Altitudes in the Pulsar Magnetosphere. *Astron. Astrophys.* **1993**, *273*, 563–569. Available online: https://ui.adsabs.harvard.edu/abs/1993A&A...273..563G (accessed on 29 November 2024).
21. Phillips, J.A. Radio Emission Altitudes in the Pulsar Magnetosphere. *Astrophys. J.* **1992**, *385*, 282. Available online: https://ui.adsabs.harvard.edu/abs/1992ApJ...385..282P (accessed on 29 November 2024). [CrossRef]
22. Blaskiewicz, M.; Cordes, J.M.; Wasserman, I. A Relativistic Model of Pulsar Polarization. *Astrophys. J.* **1991**, *370*, 643. Available online: https://ui.adsabs.harvard.edu/abs/1991ApJ...370..643B (accessed on 29 November 2024). [CrossRef]
23. Gangadhara, R.T.; Gupta, Y. Understanding the Radio Emission Geometry of PSR B0329+54. *Astrophys. J.* **2001**, *555*, 31–39. Available online: https://ui.adsabs.harvard.edu/abs/2001ApJ...555...31G (accessed on 29 November 2024). [CrossRef]
24. Kijak, J.; Gil, J. Radio Emission Altitude in Pulsars. *Astron. Astrophys.* **2003**, *397*, 969–972. Available online: https://ui.adsabs.harvard.edu/abs/2003A&A...397..969K (accessed on 29 November 2024). [CrossRef]
25. Rookyard, S.C.; Weltevrede, P.; Johnston, S. Constraints on Viewing Geometries from Radio Observations of -Ray-Loud Pulsars Using a Novel Method. *Mon. Not. R. Astron. Soc.* **2015**, *446*, 3367–3388. Available online: https://ui.adsabs.harvard.edu/abs/2015MNRAS.446.3367R/abstract (accessed on 29 November 2024). [CrossRef]
26. Xilouris, K.M.; Seiradakis, J.H.; Gil, J.; Sieber, W.; Wielebinski, R. Pulsar Polarimetric Observations at 10.55GHz. *Astron. Astrophys.* **1995**, *293*, 153–165. Available online: https://ui.adsabs.harvard.edu/abs/1995A&A...293..153X (accessed on 29 November 2024).
27. Rankin, J.M. Toward an empirical theory of pulsar emission. II. On the spectral behavior of component width. *Astrophys. J.* **1983**, *274*, 359–368. Available online: https://ui.adsabs.harvard.edu/abs/1983ApJ...274..359R (accessed on 29 November 2024). [CrossRef]
28. Thorsett, S.E. Frequency Dependence of Pulsar Integrated Profiles. *Astrophys. J.* **1991**, *377*, 263. Available online: https://ui.adsabs.harvard.edu/abs/1991ApJ...377..263T (accessed on 29 November 2024). [CrossRef]
29. Chen, J.L.; Wang, H.G. Frequency Dependence of Pulse Width for 150 Radio Normal Pulsars. *Astron. J. Suppl. Ser.* **2014**, *215*, 11. Available online: https://ui.adsabs.harvard.edu/abs/2014ApJS..215...11C (accessed on 29 November 2024). [CrossRef]
30. Shang, L.H.; Lu, J.G.; Du, Y.J.; Hao, L.F.; Li, D.; Lee, K.-J.; Li, B.; Li, L.-X.; Qiao, G.-J.; Shen, Z.-Q.; et al. Investigating the Multifrequency Pulse Profiles of PSRs B0329+54 and B1642-03 in an Inverse Compton Scattering Model. *Mon. Not. R. Astron. Soc.* **2017**, *468*, 4389–4398. Available online: https://ui.adsabs.harvard.edu/abs/2017MNRAS.468.4389S (accessed on 29 November 2024). [CrossRef]
31. Pilia, M.; Hessels, J.W.T.; Stappers, B.W.; Kondratiev, V.I.; Kramer, M.; Van Leeuwen, J.; Weltevrede, P.; Lyne, A.G.; Zagkouris, K.; Hassall, T.E.; et al. Wide-Band, Low-Frequency Pulse Profiles of 100 Radio Pulsars with LOFAR. *Astron. Astrophys.* **2016**, *586*, A92. Available online: https://ui.adsabs.harvard.edu/abs/2016A&A...586A..92P (accessed on 29 November 2024). [CrossRef]
32. Stovall, K.; Ray, P.S.; Blythe, J.; Dowell, J.; Eftekhari, T.; Garcia, A.; Lazio, T.J.W.; McCrackan, M.; Schinzel, F.K.; Taylor, G.B. Pulsar Observations Using the First Station of the Long Wavelength Array and the LWA Pulsar Data Archive. *Astrophys. J.* **2015**, *808*, 156. Available online: https://ui.adsabs.harvard.edu/abs/2015ApJ...808..156S (accessed on 29 November 2024). [CrossRef]
33. Zhao, R.-S.; Yan, Z.; Wu, X.-J.; Shen, Z.-Q.; Manchester, R.N.; Liu, J.; Qiao, G.-J.; Xu, R.-X.; Lee, K.-J. 5.0 GHz TMRT Observations of 71 Pulsars. *Astrophys. J.* **2019**, *874*, 64. Available online: https://ui.adsabs.harvard.edu/abs/2019ApJ...874...64Z (accessed on 29 November 2024). [CrossRef]
34. Rankin, J. Radio Pulsar Beam Geometry at Lower Frequencies: Bright Sources Outside the Arecibo Sky. *Mon. Not. R. Astron. Soc.* **2022**, *514*, 3202–3211. Available online: https://ui.adsabs.harvard.edu/abs/2022MNRAS.514.3202R (accessed on 29 November 2024). [CrossRef]
35. Olszanski, T.; Rankin, J.; Venkataraman, A.; Wahl, H. Pulsar Emission Beam Geometry of Radio Broad-Band Arecibo Sources. *Mon. Not. R. Astron. Soc.* **2022**, *517*, 1189–1196. Available online: https://ui.adsabs.harvard.edu/abs/2022MNRAS.517.1189O (accessed on 29 November 2024). [CrossRef]
36. Sutton, J.M. Scattering of Pulsar Radiation in the Interstellar Medium. *Mon. Not. R. Astron. Soc.* **1971**, *155*, 51. Available online: https://ui.adsabs.harvard.edu/abs/1971MNRAS.155...51S (accessed on 29 November 2024). [CrossRef]
37. Arzoumanian, Z.; Nice, D.J.; Taylor, J.H.; Thorsett, S.E. Timing Behavior of 96 Radio Pulsars. *Astrophys. J.* **1994**, *422*, 671. Available online: https://ui.adsabs.harvard.edu/abs/1994ApJ...422..671A (accessed on 29 November 2024). [CrossRef]

38. Sun, S.N.; Yan, W.M.; Wang, N.; Wang, H.G.; Wang, S.Q.; Dang, S.J. Polarimetric Observations of PSR J0614+2229 and PSR J1938+2213 Using FAST. *Astrophys. J.* **2022**, *934*, 57. Available online: https://ui.adsabs.harvard.edu/abs/2022ApJ...934...57S (accessed on 29 November 2024). [CrossRef]
39. Cañellas, A.; Joshi, B.C.; Paredes, J.M.; Ishwara-Chandra, C.H.; Moldón, J.; Zabalza, V.; Martí, J.; Ribó, M. Search for Radio Pulsations in LS I +61 303. *Astron. Astrophys.* **2012**, *543*, A122. Available online: https://ui.adsabs.harvard.edu/abs/2012A&A...543A.122C (accessed on 29 November 2024). [CrossRef]
40. Davies, J.G.; Lyne, A.G.; Smith, F.G.; Izvekova, V.A.; Kuzmin, A.D.; Shitov, I.P.; The Magnetic Field Structure of PSR 0809+74. *Mon. Not. R. Astron. Soc.* **1984**, *211*, 57–68. Available online: https://ui.adsabs.harvard.edu/abs/1984MNRAS.211...57D (accessed on 29 November 2024). [CrossRef]
41. Dike, V.; Taylor, G.B.; Dowell, J.; Stovall, K. Detecting Pulsar Polarization Below 100MHz with the Long Wavelength Array. *Mon. Not. R. Astron. Soc.* **2020**, *496*, 3623–3634. Available online: https://ui.adsabs.harvard.edu/abs/2020MNRAS.496.3623D (accessed on 29 November 2024). [CrossRef]
42. Gancio, G.; Lousto, C.O.; Combi, L.; del Palacio, S.; López Armengol, F.G.; Combi, J.A.; Garc, F.; Kornecki, P.; Müller, A.L.; Gutiérrez, E.; Hauscarriaga, F.; Mancuso, G.C. Upgraded Antennas for Pulsar Observations in the Argentine Institute of Radio Astronomy. *Astron. Astrophys.* **2020**, *633*, A84. Available online: https://ui.adsabs.harvard.edu/abs/2020A&A...633A..84G (accessed on 29 November 2024). [CrossRef]
43. Gould, D.M.; Lyne, A.G. Multifrequency Polarimetry of 300 Radio Pulsars. *Mon. Not. R. Astron. Soc.* **1998**, *301*, 235–260. Available online: https://ui.adsabs.harvard.edu/abs/1998MNRAS.301..235G (accessed on 29 November 2024). [CrossRef]
44. Hamilton, P.A.; McCulloch, P.M.; Ables, J.G.; Komesaroff, M.M. Polarization Characteristics of Southern Pulsars-I. 400-MHz Observations. *Mon. Not. R. Astron. Soc.* **1977**, *180*, 1. Available online: https://ui.adsabs.harvard.edu/abs/1977MNRAS.180....1H (accessed on 29 November 2024). [CrossRef]
45. Zhi, Q.J.; Bai, J.T.; Shang, L.H.; Xu, X.; Dang, S.J.; Li, D.; Zhang, L.; Wang, P.; Xie, X.Y.; Zhao, R.S.; Dong, A.J.; Qiao, G.J. The Single-pulse Observation of PSR B2111+46 with the Five-Hundred-meter Aperture Spherical Radio Telescope. *Astrophys. J.* **2023**, *954*, 24. Available online: https://ui.adsabs.harvard.edu/abs/2023ApJ...954...24Z (accessed on 29 November 2024). [CrossRef]
46. Izvekova, V.A.; Kuzmin, A.D.; Molofeev, V.M.; Shitov, I.P. Energy Spectra Pulse Shapes of Pulsars at Metre Wavelengths. *Ustralian J. Phys.* **1979**, *32*, 25–34. Available online: https://ui.adsabs.harvard.edu/abs/1979AuJPh..32...25I (accessed on 29 November 2024). [CrossRef]
47. Izvekova, V.A.; Malofeev, V.M.; Shitov, Y.P. Pulsar Mean Pulse Profiles at 102.5-MHZ. *Sov. Astron.* **1989**, *33*, 175. Available online: https://ui.adsabs.harvard.edu/abs/1989SvA....33..175I (accessed on 29 November 2024).
48. Izvekova, V.A.; Kuzmin, A.D.; Lyne, A.G.; Shitov, Y.P.; Smith, F.G. Frequency Dependence of Characteristics of Pulsars PSR 0031-07, 0320+39, 1133+16 and 2016+28. *Mon. Not. R. Astron. Soc.* **1993**, *261*, 865–872. Available online: https://ui.adsabs.harvard.edu/abs/1993MNRAS.261..865I (accessed on 29 November 2024). [CrossRef]
49. Johnston, S.; Kerr, M. Polarimetry of 600 Pulsars from Observations at 1.4 GHz with the Parkes Radio Telescope. *Mon. Not. R. Astron. Soc.* **2018**, *474*, 4629–4636. Available online: https://ui.adsabs.harvard.edu/abs/2018MNRAS.474.4629J (accessed on 29 November 2024). [CrossRef]
50. McSweeney, S.J.; Bhat, N.D.R.; Wright, G.; Tremblay, S.E.; Kudale, S. The Frequency-Dependent Behavior of Subpulse Drifting. I. Carousel Geometry Emission Heights of PSR B0031-07. *Astrophys. J.* **2019**, *883*, 28. Available online: https://ui.adsabs.harvard.edu/abs/2019ApJ...883...28M (accessed on 29 November 2024). [CrossRef]
51. Keith, M.J.; Johnston, S.; Levin, L.; Bailes, M. 17–24-GHz Observations of Southern Pulsars. *Mon. Not. R. Astron. Soc.* **2011**, *416*, 346–354. Available online: https://ui.adsabs.harvard.edu/abs/2011MNRAS.416..346K (accessed on 29 November 2024). [CrossRef]
52. Kramer, M. Geometrical Analysis of Average Pulsar Profiles Using Multi-Component Gaussian FITS at Several Frequencies. II. Individual Results. *Astron. Astrophys. Suppl.* **1994**, *107*, 527–539. Available online: https://ui.adsabs.harvard.edu/abs/1994A&AS..107..527K (accessed on 29 November 2024).
53. Basu, R.; Lew, o.W.; Kijak, J.; Bartosz, Ś.; Soida, M.; Błaszkiewicz, L.; Krankowski, A. Single Pulse Emission from PSR B0809+74 at 150MHz Using Polish LOFAR Station. *Mon. Not. R. Astron. Soc.* **2023**, *526*, 691–699. Available online: https://ui.adsabs.harvard.edu/abs/2023MNRAS.526..691B (accessed on 29 November 2024). [CrossRef]
54. Wang, P.F.; Han, J.L.; Xu, J.; Wang, C.; Yan, Y.; Jing, W.C.; Su, W.Q.; Zhou, D.J.; Wang, T. FAST Pulsar Database. I. Polarization Profiles of 682 Pulsars. *Esearch Astron. Astrophys.* **2023**, *23*, 104002. Available online: https://ui.adsabs.harvard.edu/abs/2023RAA....23j4002W (accessed on 29 November 2024). [CrossRef]
55. Cai, Y.; Dang, S.; Yuen, R.; Shang, L.; Kou, F.; Yuan, J.; Zhang, L.; Zhou, Z.; Wang, N.; Li, Q.; et al. The Study of Mode Switching Behavior of PSR J0614+2229 Using the Parkes Ultra-Wideband Receiver Observations. *Astrophys. J.* **2024**, *966*, 241. Available online: https://ui.adsabs.harvard.edu/abs/2024ApJ...966..241C (accessed on 29 November 2024). [CrossRef]
56. Manchester, R.N.; Taylor, J.H. Observed Derived Parameters for 330 pulsars. *Astron. J.* **1981**, *86*, 1953–1973. Available online: https://ui.adsabs.harvard.edu/abs/1981AJ.....86.1953M (accessed on 29 November 2024). [CrossRef]

57. McCulloch, P.M.; Hamilton, P.A.; Manchester, R.N.; Ables, J.G. Polarization Characteristics of Southern Pulsars - II. 640-MHz Observations. *Mon. Not. R. Astron. Soc.* **1978**, *183*, 645–676. Available online: https://ui.adsabs.harvard.edu/abs/1978MNRAS.183..645M (accessed on 29 November 2024). [CrossRef]
58. Mitra, D.; Basu, R.; Maciesiak, K.; Skrzypczak, A.; Melikidze, G.I.; Szary, A.; Krzeszowski, K. Meterwavelength Single-Pulse Polarimetric Emission Survey. *Astrophys. J.* **2016**, *833*, 28. Available online: https://ui.adsabs.harvard.edu/abs/2016ApJ...833...28M (accessed on 29 November 2024). [CrossRef]
59. Singh, S.; Gupta, Y.; De, K. Single Pulse Polarization Study of Pulsars B0950 + 08 and B1642-03: Micropulse Properties and Mixing of Orthogonal Modes. *Mon. Not. R. Astron. Soc.* **2024**, *527*, 2612–2623. Available online: https://ui.adsabs.harvard.edu/abs/2024MNRAS.527.2612S (accessed on 29 November 2024). [CrossRef]
60. Olszanski, T.E.; Mitra, D.; Rankin, J.M. Arecibo 4.5/1.4/0.33-GHz polarimetric Single-Pulse Emission Survey. *Mon. Not. R. Astron. Soc.* **2019**, *489*, 1543–1555. Available online: https://ui.adsabs.harvard.edu/abs/2019MNRAS.489.1543O (accessed on 29 November 2024). [CrossRef]
61. Page, C.G. The Drifting Sub-Pulse Phenomenon in PSR 0809+74. *Mon. Not. R. Astron. Soc.* **1973**, *163*, 29. Available online: https://ui.adsabs.harvard.edu/abs/1973MNRAS.163...29P (accessed on 29 November 2024). [CrossRef]
62. Chen, J.L.; Wen, Z.G.; Wang, Z.; Duan, X.F.; He, D.L.; Wang, N.; Wang, H.G.; Yuan, J.P.; Huang, L.; Lyu, C.B.; et al. Investigation of Periodic Modulation Behaviors from Pulsar J2022+5154. *Astrophys. J.* **2024**, *961*, 114. Available online: https://ui.adsabs.harvard.edu/abs/2024ApJ...961..114C (accessed on 29 November 2024). [CrossRef]
63. Kijak, J.; Kramer, M.; Wielebinski, R.; Jessner, A. Pulse Shapes of Radio Pulsars at 4.85 GHz. *Astron. Astrophys. Suppl.* **1998**, *127*, 153–165. Available online: https://ui.adsabs.harvard.edu/abs/1998A&AS..127..153K (accessed on 29 November 2024). [CrossRef]
64. Zhao, D.; Yan, W.M.; Wang, N.; Yuan, J.P. Investigation of Emission States of PSR J1722-3207. *Astrophys. J.* **2023**, *959*, 26. Available online: https://ui.adsabs.harvard.edu/abs/2023ApJ...959...26Z (accessed on 29 November 2024). [CrossRef]
65. Basu, R.; Mitra, D.; Melikidze, G.I. Mode Changing in PSR B0844-35 and PSR B1758-29 with Enhanced Emission at the Profile Centers. *Astrophys. J.* **2023**, *959*, 92. Available online: https://ui.adsabs.harvard.edu/abs/2023ApJ...959...92B (accessed on 29 November 2024). [CrossRef]
66. Posselt, B.; Karastergiou, A.; Johnston, S.; Parthasarathy, A.; Oswald, L.S.; Main, R.A.; Basu, A.; Keith, M.J.; Song, X.; Weltevrede, P.; et al. The Thousand Pulsar Array Program on MeerKAT-IX. The Time-Averaged Properties of the Observed Pulsar Population. *Mon. Not. R. Astron. Soc.* **2023**, *520*, 4582–4600. Available online: https://ui.adsabs.harvard.edu/abs/2023MNRAS.520.4582P (accessed on 29 November 2024). [CrossRef]
67. Tsai, J.W.; Simonetti, J.H.; Bear, B.; Gough, J.D.; Newton, J.R.; Kavic, M. Simultaneous Observations of Giant Pulses from Pulsar PSR B0031-07 AT 38MHz AND 74MHz. *Astron. J.* **2016**, *151*, 65. Available online: https://ui.adsabs.harvard.edu/abs/2016AJ....151...65T (accessed on 29 November 2024). [CrossRef]
68. van Ommen, T.D.; D'Alessandro, F.; Hamilton, P.A.; McCulloch, P.M. Polarimetric Observations of Southern Pulsars at 800 and 950MHz. *Mon. Not. R. Astron. Soc.* **1997**, *287*, 307–327. Available online: https://ui.adsabs.harvard.edu/abs/1997MNRAS.287..307V (accessed on 29 November 2024). [CrossRef]
69. Vitkevich, V.V.; Shitov, Y.P. Short Duration Pulsations of CP 0808 and Main Features of its Radio Emission in the Metre Band. *Nature* **1970**, *225*, 248–251. Available online: https://ui.adsabs.harvard.edu/abs/1970Natur.225..248V (accessed on 29 November 2024). [CrossRef]
70. Zhou, Z.R.; Wang, J.B.; Wang, N.; Hobbs, G.; Wang, S.Q. Ultra-wide Bandwidth Observations of 19 Pulsars with Parkes Telescope. *Esearch Astron. Astrophys.* **2022**, *22*, 085001. Available online: https://ui.adsabs.harvard.edu/abs/2022RAA....22h5001Z (accessed on 29 November 2024). [CrossRef]
71. Zhao, R.S.; Wu, X.J.; Yan, Z.; Shen, Z.Q.; Manchester, R.N.; Qiao, G.J.; Xu, R.X.; Wu, Y.J.; Zhao, R.B.; Li, B.; Du, Y.J. TMRT Observations of 26 Pulsars at 8.6 GHz. *Astrophys. J.* **2017**, *845*, 156. Available online: https://ui.adsabs.harvard.edu/abs/2017ApJ...845..156Z (accessed on 29 November 2024). [CrossRef]
72. Rankin, J.M. Toward an Empirical Theory of Pulsar Emission. IV. Geometry of the Core Emission Region. *Astrophys. J.* **1990**, *352*, 247. Available online: https://ui.adsabs.harvard.edu/abs/1990ApJ...352..247R (accessed on 29 November 2024). [CrossRef]
73. Rankin, J.M. Toward an Empirical Theory of Pulsar Emission. VI. The Geometry of the Conal Emission Region: Appendix and Tables. *Astron. J. Suppl. Ser.* **1993**, *85*, 145. Available online: https://ui.adsabs.harvard.edu/abs/1993ApJS...85..145R (accessed on 29 November 2024). [CrossRef]
74. Bartel, N. Evidence for Ultra Broad Band Absorption of Radio Emission in the Pulsar Magnetosphere. *Astron. Astrophys.* **1981**, *97*, 384–387. Available online: https://ui.adsabs.harvard.edu/abs/1981A&A....97..384B (accessed on 29 November 2024).
75. Xu, X.; Shang, L.H.; Zhi, Q.J.; Qiao, G.J.; Dang, S.J.; Bai, J.T.; Zhao, R.S.; Lu, J.G.; Dong, A.J.; Lin, Q.W.; Zhang, D.D.; Yang, H. A Systematic Study of the Frequency Evolution Behavior of Pulsar Pulse Profiles. *Astrophys. J.* **2021**, *917*, 108. Available online: https://ui.adsabs.harvard.edu/abs/2021ApJ...917..108X (accessed on 29 November 2024). [CrossRef]

76. Wu, X.; Gao, X.; Rankin, J.M.; Xu, W.; Malofeev, V.M. Gaussian Component Decomposition and the Five-Component Profile of Pulsar 1451–68. *Astron. J.* **1998**, *116*, 1984–1991. Available online: https://ui.adsabs.harvard.edu/abs/1998AJ....116.1984W (accessed on 29 November 2024). [CrossRef]
77. Kramer, M.; Wielebinski, R.; Jessner, A.; Gil, J.A.; Seiradakis, J.H. Geometrical Analysis of Average Pulsar Profiles Using Multi-Component Gaussian FITS at Several Frequencies. I. Method and Analysis. *Astron. Astrophys. Suppl.* **1994**, *107*, 515–526. Available online: https://ui.adsabs.harvard.edu/abs/1994A&AS..107..515K (accessed on 29 November 2024).
78. Kijak, J.; Gil, J. Radio Emission Altitudes in Pulsar Magnetospheres. *Mon. Not. R. Astron. Soc.* **1997**, *288*, 631–637. Available online: https://ui.adsabs.harvard.edu/abs/1997MNRAS.288..631K (accessed on 29 November 2024). [CrossRef]
79. Press, W.H.; Teukolsky, S.A.; Vetterling, W.T.; Flannery, B.P. *Numerical Recipes*, 3rd ed.; The Art of Scientific Computing; Cambridge University Press: Cambridge, UK, 2007.
80. Bilous, A.V.; Hessels, J.W.T.; Kondratiev, V.I.; van Leeuwen, J.; Stappers, B.W.; Weltevrede, P.; Falcke, H.; Hassall, T.E.; Pilia, M.; Keane, E.; et al. LOFAR observations of PSR B0943+10: Profile Evolution and Discovery of a Systematically Changing Profile Delay in Bright Mode. *Astron. Astrophys.* **2014**, *572*, A52. Available online: https://ui.adsabs.harvard.edu/abs/2014A&A...572A..52B (accessed on 29 November 2024). [CrossRef]
81. Wu, X.-J.; Huang, Z.-K.; Xu, X.-B. The Radial Structure of Pulsar Radio Emission Regions. *Chin. J. Astron. Astrophys.* **2002**, *2*, 454–462. Available online: https://ui.adsabs.harvard.edu/abs/2002ChJAA...2..454W (accessed on 29 November 2024). [CrossRef]
82. Mitra, D.; Li, X.H. Comparing Geometrical and Delay Radio Emission Heights in Pulsars. *Astron. Astrophys.* **2004**, *421*, 215–228. Available online: https://ui.adsabs.harvard.edu/abs/2004A&A...421..215M (accessed on 29 November 2024). [CrossRef]
83. von Hoensbroech, A.; Xilouris, K.M. Does Radius-to-Frequency Mapping Persist Close to the Pulsar Surface? *Astron. Astrophys.* **1997**, *324*, 981–987. Available online: https://ui.adsabs.harvard.edu/abs/1997A&A...324..981V (accessed on 29 November 2024).
84. Thomas, R.M.C.; Gangadhara, R.T. Absolute Emission Altitude of Pulsars: PSRs B1839+09, B1916+14, and B2111+46. *Astron. Astrophys.* **2010**, *515*, A86. Available online: https://ui.adsabs.harvard.edu/abs/2010A&A...515A..86T (accessed on 29 November 2024). [CrossRef]
85. Roy, T.; Surnis, M.; Das, R. Absolute Emission Height Determination of the Radio Emission Components of PSR B2111+46 at Multiple Bands by Relativistic Phase Shift Method. *Astrophys. Space Sci.* **2024**, *369*, 91. Available online: https://ui.adsabs.harvard.edu/abs/2024Ap&SS.369...91R (accessed on 29 November 2024). [CrossRef]
86. Rankin, J.M. The Radial Structure of Pulsar Radio Emission Regions. *Astrophys. J.* **1993**, *405*, 285. Available online: https://ui.adsabs.harvard.edu/abs/1993ApJ...405..285R/abstract (accessed on 29 November 2024). [CrossRef]
87. Kijak, J. Emission Altitudes in Young and Old Radio Pulsars. *Mon. Not. R. Astron. Soc.* **1993**, *323*, 537–541. [CrossRef]
88. Mitra, D.; Rankin, J.M. Toward an Empirical Theory of Pulsar Emission. VII. On the Spectral Behavior of Conal Beam Radii and Emission Heights. *Astrophys. J.* **2002**, *577*, 322–336. Available online: https://ui.adsabs.harvard.edu/abs/2002ApJ...577..322M (accessed on 29 November 2024). [CrossRef]
89. Shang, L.H.; Xu, X.; Dang, S.J.; Zhi, Q.J.; Bai, J.T.; Zhu, R.H.; Lin, Q.W.; Yang, H. A Simulation of Radius-frequency Mapping for PSR J1848-0123 with an Inverse Compton Scattering Model. *Astrophys. J.* **2021**, *916*, 62. Available online: https://ui.adsabs.harvard.edu/abs/2021ApJ...916...62S (accessed on 29 November 2024). [CrossRef]
90. Zhi, Q.J.; Xu, X.; Shang, L.H.; Qiao, G.J.; Bai, J.T.; Dang, S.J.; Zhao, R.S.; Dong, A.J.; Zhang, D.D.; Lin, Q.W.; Yang, H. Frequency Evolution Behavior of Pulse Profile of PSR B1737+13 with the Inverse Compton Scattering Model. *Astrophys. J.* **2022**, *926*, 73. Available online: https://ui.adsabs.harvard.edu/abs/2022ApJ...926...73Z (accessed on 29 November 2024). [CrossRef]